Universiteit
Leiden
The Netherlands

Probing new physics in the laboratory and in space

Ovchynnikov, M.

Citation

Ovchynnikov, M. (2021, December 14). *Probing new physics in the laboratory and in space*. *Casimir PhD Series*. Retrieved from https://hdl.handle.net/1887/3247187

Version:	Publisher's Version
License:	Licence agreement concerning inclusion of doctoral thesis in the Institutional Repository of the University of Leiden
Downloaded from:	https://hdl.handle.net/1887/3247187

Note: To cite this publication please use the final published version (if applicable).

Chapter 2

Accelerator and laboratory searches[1]

In this chapter, we consider searches for FIPs at accelerator experiments. We first re-analyze the bounds from the past experiment CHARM on HNLs, demonstrating for the first time that the actual bounds are stronger by a factor of few (for the e/μ mixing) to a few orders of magnitude (for the τ mixing), in dependence on the mixing pattern, see Sec. 2.1. Next, we consider the searches for FIPs using the displaced vertices scheme at the LHC, and in particular the search with muon trackers at CMS, see Sec. 2.2. Finally, we proceed to experiments that search FIPs via their scattering, and estimate the potential of SND@LHC to search for scatterings of Light Dark Matter particles off nucleons, see Sec. 2.3.

2.1 Bounds on HNLs from CHARM experiment

In order to define the target parameter space for Intensity Frontier experiments for a given model, we need to know constraints on it coming from past experiments.

Let us look closer at constraints on HNLs. The bounds on HNLs in the GeV mass range that mix purely with electron and tau neutrino flavors as reported in [36] are shown in Fig. 2.1.

For the e mixing, below the kaon mass HNLs may be produced in decays $K \to N + e$ of copiously produced kaons, and thus are severely constrained by kaon fabrics (T2K, NA62). Being combined with the parameter space excluded by BBN, they practically rule out light HNLs. To search for heavier HNLs, we need D ($m_N < m_{D_s} \approx 1.97$ GeV), B mesons ($m_N < m_{B_c} \approx 6.3$ GeV), or W/Z bosons ($m_N < m_Z \approx 91$ GeV) in order to produce them. The amounts of these particles at experiments are much lower than amounts of kaons, and constraints are much weaker. In particular, in the mass range $m_N < m_{D_s}$ the strongest current bound comes from an old experiment CHARM, which was an SPS-based

[1] Results of this chapter are presented in papers [56–58]. The main contribution of Maksym Ovchynnikov to them are analytic estimates, simulations, and the main idea in [58].

beam dump experiment which searched for displaced decays into a di-lepton pair:

$$N \to e^+e^-, \quad N \to \mu^+\mu^-, \quad N \to \mu^\pm e^\mp \tag{2.1.1}$$

Larger masses are constrained by DELPHI experiment, which was a e^+e^- collider at energies equal to m_Z.

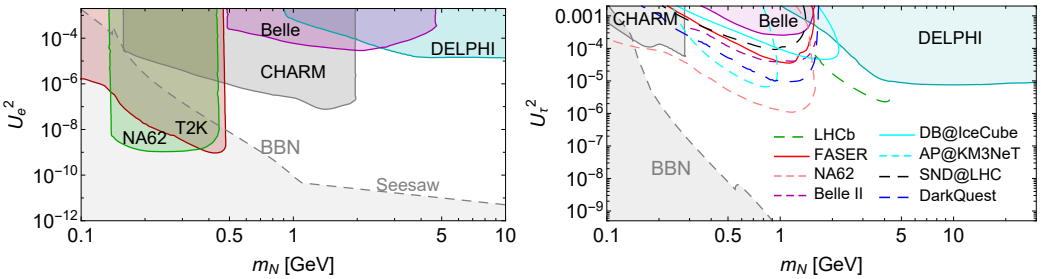

Figure 2.1: The parameter space of HNLs with the pure e (the left panel) and τ (the right panel) mixing. Constraints from the previous experiments – NA62, T2K, Belle, CHARM, DELPHI – are shown as reported in [36]. We do not show sub-dominant bounds coming from past experiments, such as NOMAD [59] and ArgoNeuT [60] for the τ mixing. For the pure τ mixing, we do not show the constraints imposed by the T2K experiment [61], since they are reported for non-zero couplings $U_{e/\mu}$ which dominate the production Constraints from the CHARM experiment are taken from the literature [62, 63], while our re-analysis for them is shown in Fig. 2.6. The light gray domain corresponds to couplings that are either excluded by BBN [37, 64] or too small to provide active neutrino masses. For the pure τ mixing, we also show sensitivities of the next generation Intensity Frontier experiments (see text for details). In cyan, we show HNL parameter space that may be probed by neutrino observatories: the solid line shows the sensitivity of IceCube to the "double bang" signature from [65], while the dashed line corresponds to the sensitivity of KM3NeT to decays of HNLs produced in the atmosphere, see text and Sec. 2.1.5 for details.

For the τ mixing, constraints at mass $m_N < m_{D_s}$ are very different, being much weaker than for the e mixing. Such HNLs cannot be constrained by kaon fabrics, as the production channel $K \to \tau + N$ is kinematically impossible. Next, constraints from CHARM are restricted by mass $m_N < 290$ MeV, with no clear reason provided. This result looks suspicious

As a result, the mass range 210 MeV $< m_N < m_D$ is reported as a poorly constrained domain, which is a reason of numerous experiments proposed to probe the unexplored parameter space: displaced decays at FASER [66, 67], Belle II [68], SND@LHC [57], DarkQuest [69], and NA62 in the dump mode [67]; prompt decays at LHCb [70, 71]; and double bang signature at IceCube, SuperKamiokande, DUNE and HyperKamiokande [65, 72].

The planned neutrino observatory KM3NeT [73] working as an atmospheric beam dump may have sensitivity to such HNLs as well. Namely, HNLs may be produced in numerous collisions of cosmic protons with atmospheric particles, then reach the detector

volume located deeply underwater in the Mediterranean Sea, and further decay into a dimuon pair inside. Such combination of decay products may be in principle distinguished from the SM events due to neutrino scatterings and penetrating atmospheric muons. We discuss this signature in more detail and estimate the sensitivity of KM3NeT to HNLs produced in the atmosphere in Sec. 2.1.5, and make the conclusions in Sec. 2.1.4.

Constraints from the CHARM experiment as reported in the literature for HNL that mix purely with e/μ and τ neutrinos are very different, with no reason provided.

In this section, we re-analyze the bounds from the CHARM experiment. We study the HNL decay channel $N \to e^+e^-\nu/\mu^+\mu^-\nu$ and show for the first time that, in addition to the constraints on the HNL's mixings with ν_e or ν_μ, the same data also implies limits on the HNLs that mix only with ν_τ and have masses in the range $290\,\mathrm{MeV} < m_N \lesssim 1.6\,\mathrm{GeV}$.

The CHARM bounds re-analysis presented in this chapter may be similarly applied for the re-analysis of bounds coming from the NOMAD experiment [59]. However, due to the smaller intensity of the proton beam at NOMAD and simultaneously similar geometric acceptance of the decay volume, the bounds imposed by NOMAD are sub-dominant, and we therefore do not make the re-analysis in this work.

2.1.1 CHARM experiment

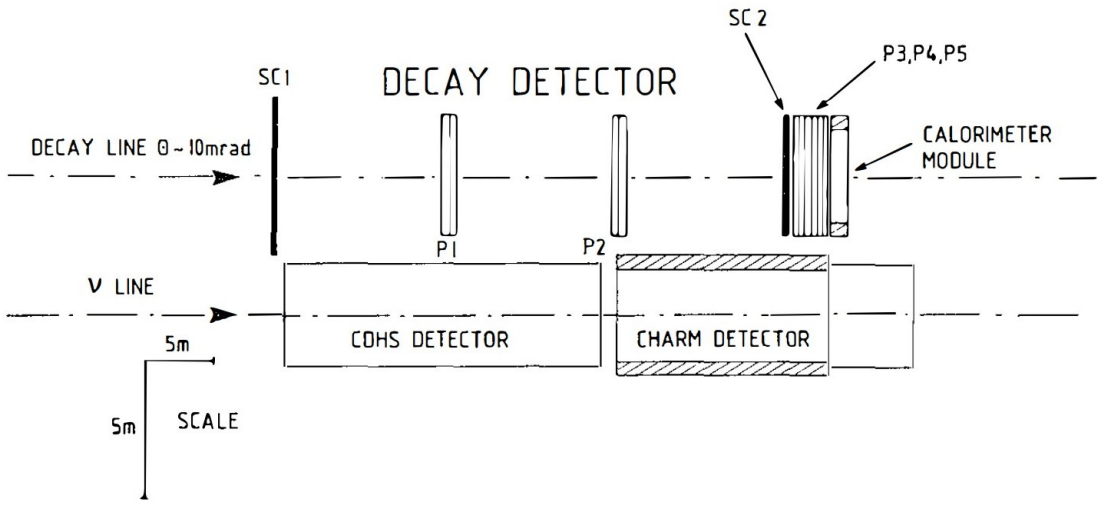

Figure 2.2: The layout of the CHARM facility, adopted from [62].

The CHARM experiment [62, 74] was a proton beam dump operating at the 400 GeV CERN SPS. The total number of exposed protons was split into $1.7 \cdot 10^{18}$ protons on a solid copper target and $0.7 \cdot 10^{18}$ on a laminated copper target with the $1/3$ effective density. Searches for decays of HNLs were performed in the $l_{\text{fid}} = 35\,\mathrm{m}$ long decay region (see Fig. 2.2) defined by the two scintillator planes SC1 and SC2, located at the distance

$l_{\text{min}} = 480\,\text{m}$ from the copper target. The decay detector covered the $3.9 \cdot 10^{-5}\,\text{sr}$ solid angle and had the transverse dimensions $3 \times 3\,\text{m}^2$, with the center displaced by $5\,\text{m}$ from the axis. The fine-grain calorimeter at CHARM was aimed to detect inelastic scattering of electrons and muons produced in hypothetical decays of HNLs [75]. The sets of tube planes P1-P5 [76] were installed to improve the reconstruction of the decay vertex and the angular resolution.

2.1.2 Bounds of CHARM on HNLs as reported in literature

As we have already discussed, in the GeV mass range, the constraints on the mixing angle U_τ^2 are orders of magnitude weaker as compared to the constraints on $U_{e/\mu}^2$ (constraints for the μ mixing are similar to the ones for the e mixing), see Fig. 2.1. Namely, for the e/μ mixing, the large values of the couplings for HNLs with masses $m_K \lesssim m_N \lesssim m_D \simeq 2\,\text{GeV}$ are excluded by the CHARM experiment [62, 74], while for the τ mixing CHARM constraints on U_τ are reported in the literature only for masses $m_N < 290\,\text{MeV}$.

The reason is the following: the original analysis [62, 74] is based on negative results for searches for decays of feebly interacting particles into one of the possible dilepton pair – $\mu e, \mu\mu, \mu e$. For HNLs, they consider only decays mediated through the charged current (CC) interaction (see Fig. 2.3, diagram (a)) that give rise to leptonic decays

$$N_\alpha \to l_\alpha \bar{l}_\beta \nu_\beta, \quad \beta = e, \mu, \tau \tag{2.1.2}$$

If only CC interactions are taken into account, the search is suitable to constrain the mixing of HNLs with ν_e and ν_μ. To search for CC mediated decays via the τ mixing (which necessarily include a τ lepton), the HNL mass should be $m_N > m_\tau \simeq m_D$ in this model. Such HNLs are mainly produced in decays of heavy B mesons, the number of which at CHARM is insufficient to provide enough events for the couplings that are not excluded (see Fig. 2.1). Therefore, HNLs that mix only with ν_τ cannot be constrained by CHARM data using only the decays via CC.

In order to constrain the τ mixing angles of the light HNLs $m_N < m_\tau$, one should include the interactions via the neutral current (NC) into the analysis, see Fig. 2.3 (diagram (b)). In this case, the dileptonic decays are

$$N_\alpha \to \nu_\alpha l_\beta \bar{l}_\beta, \tag{2.1.3}$$

and do not require the creation of a τ lepton for the pure τ mixing.

The works [63, 77, 78] have re-analyzed the CHARM constraints on HNLs by including also the neutral current processes. However, their analysis was insufficient to put the bounds on the pure τ mixing in GeV mass range. Namely, the work [63] (the results of which are used in [36]) has limited the study of the mass range by $m_N < 290\,\text{MeV}$, while [77, 78] considered the decays of HNLs via neutral currents but did not include the production of

HNLs from τ lepton (the diagrams (c) and (d) in Fig. 2.4). As a result, these works did not report any CHARM limits on the pure τ mixing.

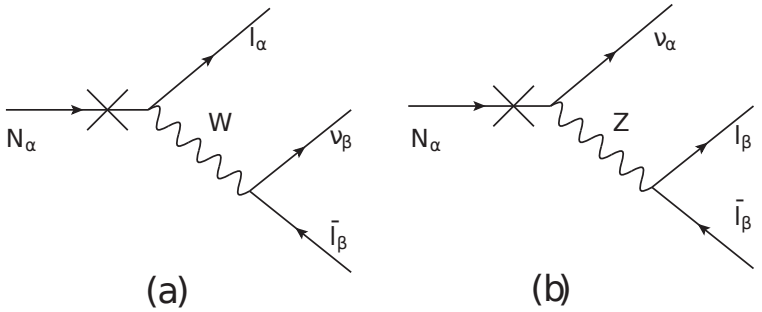

Figure 2.3: Diagrams of leptonic decays of an HNL that mixes purely with ν_α via the charged (the left diagram) and the neutral current (the right diagram).

2.1.3 Phenomenology of HNLs at CHARM

2.1.3.1 Production

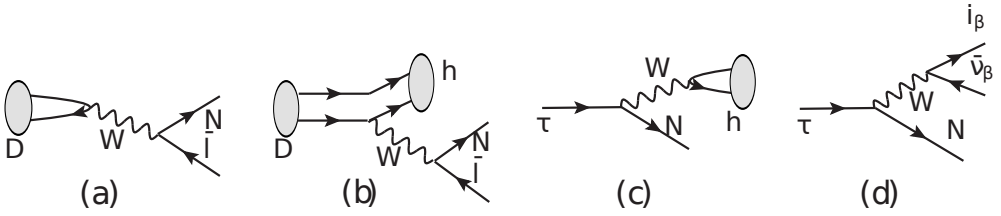

Figure 2.4: Diagrams of HNL production in leptonic and semileptonic decays of D mesons: $D_s, D^0, D^\pm$ (diagrams (a), (b)), and τ lepton, which is produced in decays of D_s meson only (diagrams (c), (d)).

At the SPS energy of $400\,\mathrm{GeV}$, HNLs with mass at the GeV scale may be produced directly either in the proton-target collisions, or in the decays of secondary particles: B, D mesons and τ leptons. The direct HNL production competes with strong interaction processes, while the production from secondary particles – with weak interactions. As a result, the latter process is dominant even taking into account small production probability of mesons [39], and the former may be completely neglected. However, similarly to the other experiment operating at SPS – NA62 in the dump mode, the CHARM experiment has no sensitivity to the HNLs produced from B mesons, implying the lower bound on the probed mass $m_N \lesssim m_{D_s} \simeq 2\,\mathrm{GeV}$.[2]

[2]To search for HNLs created in the decays of B mesons at SPS, an experiment like SHiP [20] with significantly larger beam intensity delivered to the experiment and much better geometrical acceptance would be required.

Therefore, at CHARM, HNLs may be produced only in decays of D mesons and τ leptons.

Let us define the HNL that mixes only with ν_α by N_α. Neglecting the direct production channels, the total number of N_α produced at CHARM is given by:

$$\mathcal{N}_{\text{prod}}^{(\alpha)} = 2\mathcal{N}_{c\bar{c}} \cdot \Big[\sum_{D_i} f_{c\to D_i} \text{Br}(D_i \to N_\alpha X) + \\ + f_{c\to D_s} \cdot \text{Br}(D_s \to \tau\bar{\nu}_\tau) \cdot \text{Br}(\tau \to N_\alpha X) \Big], \quad (2.1.4)$$

with $\mathcal{N}_{c\bar{c}}$ being the total number of quark-antiquark $c\bar{c}$ pairs produced at CHARM, $D_i = D^\pm$, D^0, D_s, and $f_{c\to D_i}$ the corresponding quark fragmentation fractions at SPS. The first term in the brackets describes the production from decays of D mesons (diagrams (a), (b) in Fig. 2.4) and the second – from τ leptons in the $D_s \to \tau \to N$ decay chain (diagrams (c), (d) in Fig. 2.4). $\text{Br}(D_i \to N_\alpha X)$, $\text{Br}(\tau \to N_\alpha X)$ are the branching ratios.

The amount of τ leptons is suppressed as compared to the number of D mesons, and therefore the production channel from τ is subdominant.

Indeed, the second term in Eq. (2.1.4) includes a small factor $f_{c\to D_s} \cdot \text{Br}(D_s \to \tau\bar{\nu}_\tau) \simeq 5 \cdot 10^{-3}$; for the given HNL mass, it is suppressed as compared to the first term as soon as the production from D is allowed.

The original analysis of the CHARM collaboration [62, 74] considered the mixing $\alpha = e, \mu$, for which decays from D mesons are possible for any mass in the range $m_N <$

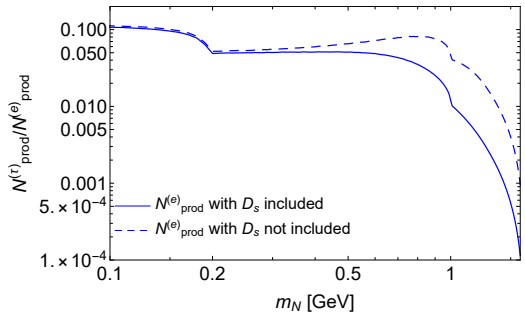

Figure 2.5: The HNL mass dependence of the ratio of the numbers of produced HNLs with pure τ and e mixing $N_{\text{prod}}^{(\tau)}/N_{\text{prod}}^{(e)}$, see Eq. (2.1.5), assuming the same values of the mixing angles $U_e^2 = U_\tau^2$ for the two models. The solid line corresponds to $N_{\text{prod}}^{(e)}$ calculated keeping the production from all D mesons D^+, D^0, D_s, while the dashed line corresponds to the estimate of $N_{\text{prod}}^{(e)} \equiv N_{\text{prod}}^{\text{CHARM}}$ calculated without the contribution of D_s, as has been done in the analysis [62] by the CHARM collaboration (see text for details).

$m_{D_s} - m_{l_\alpha} \approx 1.9\,\mathrm{GeV}$, and the production from τ decays may be completely neglected, according to the discussion above. For the τ mixing, however, the kinematic threshold of the production from D, $D_s \to \tau + N$, is $m_{D_s} - m_\tau \approx 190\,\mathrm{MeV}$, and only the second summand in Eq. (2.1.4) contributes for heavier HNLs.

Let us estimate how many HNLs with τ mixing are produced as compared to those with e mixing.

The amount of produced HNLs with the pure τ mixing ranges from 10^{-3} to 10^{-1} of those with the e mixing.

Indeed, from (2.1.4), the ratio $N^{(\tau)}_{\text{prod}}/N^{(e)}_{\text{prod}}$ is

$$\frac{N^{(\tau)}_{\text{prod}}}{N^{(e)}_{\text{prod}}} = \frac{\sum_{D_i} f_{c\to D_i}\text{Br}(D_i \to N_\tau X) + f_{c\to D_s}\text{Br}(D_s \to \tau\bar{\nu}_\tau)\text{Br}(\tau \to N_\tau X)}{\sum_{D_i} f_{c\to D_i}\text{Br}(D_i \to N_e X)}, \quad (2.1.5)$$

Assuming the same values of mixing angles $U_e^2 = U_\tau^2$ for the two models with pure e/τ mixing, the ratio $\text{Br}(\tau \to N_\tau X)/\sum f_{c\to D}\text{Br}(D \to N_e X)$ varies in the $1 - 10$ range for masses $m_N \lesssim 1.3\,\mathrm{GeV}$ and quickly drops at the kinematic threshold $m_N \approx m_\tau$ [39]. In particular, for masses $m_N \gtrsim 800\,\mathrm{MeV}$, where the dominant contribution to the HNL production with e mixing comes from D_s, we have

$$\frac{N^{(\tau)}_{\text{prod}}}{N^{(e)}_{\text{prod}}} \approx \text{Br}(D_s \to \tau\bar{\nu}_\tau) \cdot \frac{\text{Br}(\tau \to N_\tau X)}{\text{Br}(D_s \to N_e X)} < 4 \cdot 10^{-2} \quad (2.1.6)$$

The mass dependence of the ratio $N^{(\tau)}_{\text{prod}}/N^{(e)}_{\text{prod}}$ obtained from Eq. (2.1.5) is shown in Fig. 2.5.

In the original analysis [62], as well as in the re-analyses [77, 78], the production from D_s (which is the main production channel for the e and μ mixings) has not been taken into account for the e mixing.

In the mass range $m_N \gtrsim 800\,\mathrm{MeV}$, this leads to the underestimate of the number of produced HNLs, $N^{\text{CHARM}}_{\text{prod}}$, by a factor $1/6$ (see Fig. 2.4, where we show the ratio $N^{(\tau)}_{\text{prod}}/N^{\text{CHARM}}_{\text{prod}}$).

2.1.3.2 Decays and their detection

For a given number of produced HNLs, the number of detected events $N^{(\alpha)}_{\text{events}}$ for the given mixing α depends on

1. **Geometrical factors** – in order to be detected, produced HNLs need to point in the angular coverage of the CHARM decay volume, decay inside it, and their decay

products must then reach the detector and be successfully reconstructed. These factors are: geometrical acceptance ϵ_{geom}, i.e. the fraction of produced HNLs traveling in the direction of the CHARM detector; the mean HNL gamma factor γ_N; the decay acceptance ϵ_{decay}, i.e. the fraction of HNL decay products that point to the CHARM detector for HNLs that decay inside the fiducial volume.

2. The **branching ratio** $\text{Br}(N_\alpha \to l^+ l'^- \nu)$ of the channels $N_\alpha \to e^+ e^- \nu, \quad N_\alpha \to \mu^+ \mu^- \nu, \quad N_\alpha \to e^- \mu^+ \nu$ (and their charge conjugated counterparts) used for detection at CHARM [62].

The formula for $N^{(\alpha)}_{\text{events}}$ is:

$$N^{(\alpha)}_{\text{events}} = N^{(\alpha)}_{\text{prod}} \cdot \epsilon^{(\alpha)}_{\text{geom}} \cdot \sum_{l,l'=e,\mu} P^{(\alpha)}_{\text{decay}} \cdot \text{Br}(N_\alpha \to l l' \nu) \cdot \epsilon_{\text{det},ll'} \cdot \epsilon^{(\alpha)}_{\text{decay}}, \tag{2.1.7}$$

where $P^{(\alpha)}_{\text{decay}} = e^{-l_{\text{min}}/c\tau^{(\alpha)}_N \gamma^{(\alpha)}_N} - e^{-(l_{\text{min}}+l_{\text{fid}})/c\tau^{(\alpha)}_N \gamma^{(\alpha)}_N}$ is the decay probability, and $\epsilon_{\text{det},ll'}$ is the reconstruction efficiency for the given channel.

> Geometrical factors determining the sensitivity are the same for e, μ and τ mixing, while the branching ratio is smaller for the τ mixing channels, as in the former case both decays via the charged and neutral currents are relevant, while in the latter only the neutral current contribute.

Let us start by considering the lower bound of the sensitivity of the CHARM experiment, i.e. the minimal mixing angles that it may probe (the upper bound will be discussed in Sec. 2.1.4). In this regime, the decay length of the HNL $c\tau^{(\alpha)}_N \gamma^{(\alpha)}_N$ is much larger than the geometric scale of the experiment, $c\tau^{(\alpha)}_N \gamma^{(\alpha)}_N \gg l_{\text{min}} + l_{\text{fid}} \approx 515\,\text{m}$. Then $P^{(\alpha)}_{\text{decay}} \approx \frac{l_{\text{fid}}}{c\gamma^{(\alpha)}_N} \cdot \Gamma(N_\alpha)$, where $\Gamma(N_\alpha)$ is the total decay width, and it is convenient to rewrite Eq. (2.1.7) in the form

$$N^{(\alpha)}_{\text{events}} \approx N^{(\alpha)}_{\text{prod}} \times \epsilon^{(\alpha)}_{\text{geom}} \cdot \sum_{l,l'=e,\mu} \frac{l_{\text{fid}}}{c\gamma^{(\alpha)}_N} \cdot \Gamma(N_\alpha \to l l' \nu) \epsilon_{\text{det},ll'} \cdot \epsilon^{(\alpha)}_{\text{decay}}, \tag{2.1.8}$$

where $\Gamma(N_\alpha \to l^+ l'^- \nu)$ is the decay width into the dilepton pair ll'.

We will first discuss the difference in $\Gamma(N_\alpha \to l^+ l'^- \nu)$ between the cases of e and τ mixings. Decays into dileptons occur via charged and neutral current, see Fig. 2.3. For the NC mediated processes, the kinematic threshold $m_N > 2m_e \approx 1\,\text{MeV}$ is mixing-independent. In contrast, for the CC mediated process for the τ mixing this threshold is $m_N > m_\tau + m_e \approx 1.77\,\text{GeV}$, and HNLs lighter than τ lepton may decay into dileptons only via NC.

Decay widths for the processes $N_\alpha \to l^+ l'^- \nu$, assuming $m_N \gg m_l + m_{l'}$, may be

given in the unified form

$$\Gamma(N_\alpha \to l^+ l'^- \nu) = c_{ll'\nu}^{(\alpha)} \frac{G_F^2 m_N^5}{192\pi^3}, \tag{2.1.9}$$

where the coefficients $c_{ll'\nu}^{(\alpha)}$ are given in Table 2.1 [39]. For N_e, the largest decay width is $\Gamma(N_e \to \mu^+ e^- \nu_\mu)$, where only CC contributes. The width $\Gamma(N_e \to e^+ e^- \nu_e)$ is smaller:

$$\Gamma(N_e \to e^- e^+ \nu_e)/\Gamma(N_e \to e^- \mu^+ \nu_\mu) \approx 0.59, \tag{2.1.10}$$

because both NC and CC contribute in this process and interfere destructively. The smallest width is $\Gamma(N_e \to \mu^+ \mu^- \nu_e)$, with the process occurring only via NC. For N_τ, there is no process $N_\tau \to e\mu\nu$, while in the process $N_\tau \to e^+ e^- \nu_\tau$ only NC contributes, and thus the width is smaller than for N_e:

$$\Gamma(N_\tau \to e^+ e^- \nu_\tau)/\Gamma(N_e \to e^+ e^- \nu_e) \approx 0.22 \tag{2.1.11}$$

For the decay into a dimuon pair, we have $\Gamma(N_\tau \to \mu^+ \mu^- \nu_\tau) = \Gamma(N_e \to \mu^+ \mu^- \nu_e)$.

As a result, for $m_N \gg m_\mu$ the ratio of the factors $\sum_{l,l'} \Gamma(N_\alpha \to l l' \nu) \epsilon_{\text{det},ll'}$ entering Eq. (2.1.8) is given by

$$\frac{\sum_l \Gamma(N_\tau \to ll) \epsilon_{\text{det},ll}}{\sum_{l,l'} \Gamma(N_e \to ll') \epsilon_{\text{det},ll'}} \approx 0.16 \tag{2.1.12}$$

Here and below, we use the values of the efficiencies $\epsilon_{\text{det},ll'}$ as reported in [62] for the HNL mass $m_N = 1\,\text{GeV}$: $\epsilon_{\text{det},ee} = 0.6$, $\epsilon_{\text{det},e\mu} = 0.65$, $\epsilon_{\text{det},\mu\mu} = 0.75$.

In the original analysis of the sensitivity to the e mixing by the CHARM collaboration [62, 74], the Dirac nature of HNLs has been assumed (the decay widths are twice smaller), and only the CC interactions have been considered. Instead of Eq. (2.1.12), the ratio becomes

$$\frac{2\sum_l \Gamma(N_\tau \to ll) \epsilon_{\text{det},ll}}{\sum_{l,l'} \Gamma_{\text{CC}}(N_e \to ll') \epsilon_{\text{det},ll'}} \approx 0.27 \tag{2.1.13}$$

Process	$c_{ll'\nu}^{(\alpha)}$
$N_{e/\tau} \to \mu^+ \mu^- \nu_{e/\tau}$	$\frac{1}{4}(1 - 4\sin^2\theta_W + 8\sin^4\theta_W) \approx 0.13$
$N_\tau \to e^+ e^- \nu_\tau$	$\frac{1}{4}(1 - 4\sin^2\theta_W + 8\sin^4\theta_W) \approx 0.13$
$N_e \to e^- \mu^+ \nu_\mu$	1
$N_e \to e^+ e^- \nu_e$	$\frac{1}{4}(1 + 4\sin^2\theta_W + 8\sin^4\theta_W) \approx 0.59$
$N_e \to e^+ e^- \nu_e$ (CC)	1

Table 2.1: The values of $c_{ll'\nu}^{(\alpha)}$ in Eq. (2.1.9) for different decay processes. For the process $N_e \to e^+ e^- \nu_e$, we also provide the value obtained if including the charged current (CC) contribution only – the assumption used in [62].

Let us now discuss geometric factors $\epsilon_{\text{geom}}, \gamma_N, \epsilon_{\text{decay}}$. It turns out that they depend

on the mixing pattern weakly, and as a result the geometry does not influence the relative yield of events for e and τ mixing. Indeed, as was mentioned in Sec. 2.1.3.1, HNLs with τ mixing are produced in decays of τ leptons, that originate from decays of D_s. Since $m_\tau \simeq m_{D_s}$, the angle-energy distribution of τ leptons is the same as of D_s (and hence also other D mesons), whose decays produce HNLs with e mixing. The kinematics of the HNL production from D and τ is similar: two-body decays (a), (c) and three-body decays (b), (d) in Fig. 2.4 differ mainly be the replacement a neutrino or a lepton with a hadron $h = \pi, K$. However, since $m_h \ll m_{\tau,D}$, the replacement does not lead to the difference in the distribution of produced HNLs. In addition, heavy HNLs with masses $m_N \simeq 1\,\mathrm{GeV}$ share the same distribution as their mother particles, and any difference disappear. Therefore, the values ϵ_{geom}, γ_N for different mixing are the same with good precision. Next, HNL decays contain the same final states independently of the mixing, and ϵ_{decay} can also be considered the same.

To summarize, the ratio $N^{(\tau)}_{\text{events}}/N^{(e)}_{\text{events}}$ is determined only by the difference in phenomenological parameters – $N^{(\alpha)}_{\text{prod}}$ and $\Gamma(N_\alpha \to ll'\nu)$:

$$\frac{N^{(\tau)}_{\text{events}}}{N^{(e)}_{\text{events}}} \simeq \frac{N^{(\tau)}_{\text{prod}}}{N^{(e)}_{\text{prod}}} \times \frac{\sum_l \Gamma(N_\tau \to ll\nu)\epsilon_{\text{det},ll}}{\sum_{l,l'} \Gamma(N_e \to ll'\nu)\epsilon_{\text{det},ll'}} \tag{2.1.14}$$

The total number of events for the τ mixing is $10^2 - 10^4$ times smaller than for the e mixing.

To compare with the estimate of the number of events for the e mixing made by the CHARM collaboration in [62], $N^{\text{CHARM}}_{\text{events}}$, we need to take into account their assumptions on the description of HNL production and decays (see the discussion around Eqs. (2.1.5) and (2.1.13)). The resulting ratio is

$$\frac{N^{(\tau)}_{\text{events}}}{N^{\text{CHARM}}_{\text{events}}} \simeq \frac{N^{(\tau)}_{\text{prod}}}{N^{\text{CHARM}}_{\text{prod}}} \cdot \frac{2\sum_l \Gamma(N_\tau \to ll\nu)\epsilon_{\text{det},ll}}{\sum_{l,l'} \Gamma_{\text{CC}}(N_e \to ll'\nu)\epsilon_{\text{det},ll'}} \tag{2.1.15}$$

2.1.4 Results

Let us now derive the CHARM sensitivity to the τ mixing. In [62], it has been shown that the dilepton decay signature at CHARM is background free. Therefore, 90% CL sensitivity to each mixing is given by the condition

$$N^{(e,\mu,\tau)}_{\text{events}} > 2.3 \tag{2.1.16}$$

Let us define $U^2_{\text{lower,CHARM}}$ as the smallest mixing angle for which the condition (2.1.16) is satisfied for the assumptions of the original analysis of [62] (see the discussion above Eq. (2.1.15)). As the number of detected events at the lower bound $N^{(\alpha)}_{\text{events}}$ scales with the

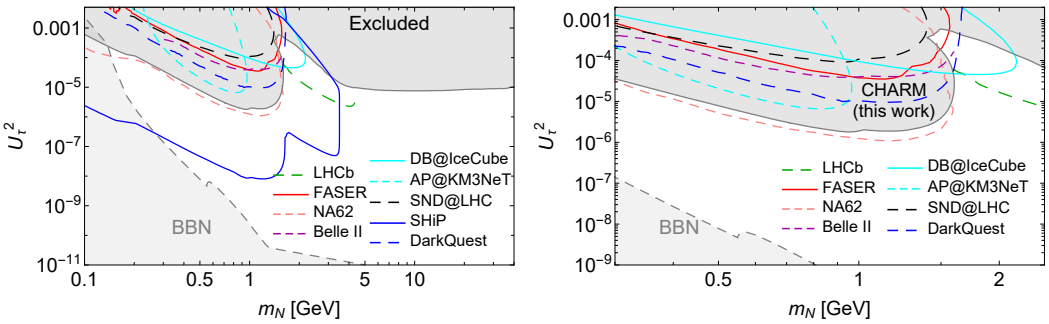

Figure 2.6: Parameter space of a single Majorana HNL that mixes with ν_τ. The excluded region is a combined reach of the DELPHI [79], T2K [61] and CHARM experiments (our result). Bounds from BBN are reproduced from [37, 64]. The sensitivity of future experiments is also shown (see text around Fig. 2.1 for details). The top panel covers the HNL mass region $m_N = 0.1 - 35\,\text{GeV}$, while the bottom panel is a zoom-in of the mass domain $m_N = \mathcal{O}(1\,\text{GeV})$.

mixing angle as $N_{\text{events}}^{(\alpha)} \propto U_\alpha^4$ (where U_α^2 comes from the production and another U_α^2 from decay probability), we can use Eqs. (2.1.15) and (2.1.5) to obtain the lower bound of the sensitivity to the τ mixing, $U^2_{\tau,\text{lower}}$, by rescaling the results reported in [62]:

$$\frac{U^4_{\tau,\text{lower}}}{U^{4\,\text{CHARM}}_{\text{lower}}} \simeq \frac{N^{\text{CHARM}}_{\text{prod}}}{N^{(\tau)}_{\text{prod}}} \cdot \frac{\sum_{l,l'} \Gamma_{\text{CC}}(N_e \to l l' \nu) \epsilon_{\text{det},ll'}}{\sum_l \Gamma(N_\tau \to l \bar{l} \nu) \epsilon_{\text{det},ll}}\bigg|_{U_e = U_\tau} . \tag{2.1.17}$$

Using the ratio $N^{\text{CHARM}}_{\text{prod}}/N^{(\tau)}_{\text{prod}}$ from Eq. (2.1.5) (see also Fig. 2.5), and the ratio of decay widths from Eq. (2.1.13), we may compare the lower bounds of the excluded regions for HNLs with e and τ mixing.

We conclude that in the mass range $m_N > 200\,\text{MeV}$ the lower bound for the τ mixing is a factor $10 - 100$ weaker than the lower bound for the e mixing reported in [62].

In the domain $m_{D_s} - m_\tau < m_N < 290\,\text{MeV}$, we validate the rescaled bound (2.1.17) by comparing it with the CHARM sensitivity to the τ mixing from [63], see Appendix 2.A.

Also, we compare our estimate for the e mixing with the CHARM sensitivity to the e mixing from [62]. In our estimates, we include neutral current interactions, the production from D_s mesons, and assume that HNLs are Majorana particles. In our estimates, we include neutral current interactions, the production from D_s mesons, and assume that HNLs are Majorana particles.

We find that for small mixing angles U_e and above $m_N \gtrsim 1\,\text{GeV}$, the bound imposed by CHARM on the e mixing may be actually improved by up to a factor $3 - 4$ as compared to [62].

At the *upper bound of the sensitivity*, the dependence of the number of events on U_α^2 is complicated and the sensitivity cannot be obtained by rescaling the results of [62]. Therefore, we independently compute the number of decay events at CHARM for HNLs with e and τ mixing and then calculate the sensitivity numerically using Eq. (2.1.16), see Appendix 2.A. In order to validate this estimate, we compare the resulting sensitivity for the τ mixing with the rescaled bound (2.1.17), and find that they are in very good agreement (Fig. 2.27).

Let us comment on errors of our estimates. We used the values of reconstruction efficiencies $\epsilon_{\text{rec},ll}$ reported in [62] for the HNL mass $m_N = 1\,\text{GeV}$. Hence, the calculation may be further refined by including HNL mass dependent reconstruction efficiencies. However, as the study [63] performed for the τ mixing and masses $m_N < 290\,\text{MeV}$ has shown similar efficiency, we do not expect any significant changes.

Our final results for the τ mixing are given in Fig. 2.6, where we show the domain excluded by previous experiments together with updated CHARM bounds, and the sensitivity of the future experiments mentioned in Sec. 2.1, together with SHiP [80]. Comparing with Fig. 2.1, we find that in the mass range $380\,\text{MeV} < m_N < 1.6\,\text{GeV}$ our results improve previously reported bounds on the mixing angle U_τ^2 by two orders of magnitude. In particular, it excludes large part of the parameter space that was suggested to be probed by the future experiments. For instance, Belle II, FASER, DarkQuest and IceCube have sensitivity only in the narrow domain above the CHARM upper bound, while NA62 may slightly push probed angles to lower values. Significant progress in testing the mixing of HNLs with ν_τ can be achieved by LHCb, which probes the complementary mass range $m_N > 2\,\text{GeV}$, and dedicated Intensity Frontier experiments, with SHiP being optimal for searches of HNLs from decays of D mesons and τ leptons.

2.1.5 Comparison with atmospheric beam dumps

Apart from the production at accelerators, HNLs with masses in GeV range may be numerously produced in decays of τ leptons, originated from the collisions of high-energy cosmic protons with the well-known spectrum [81]

$$\frac{d\Phi}{d\Omega dt dS dE_p} \approx \begin{cases} 1.7\; E_{p,\,\text{GeV}}^{-2.7}\;\text{GeV}^{-1}\text{sr}^{-1}\text{cm}^{-2}\text{s}^{-1}, & E_p < 5\cdot 10^6\,\text{GeV} \\ 174\; E_{p,\,\text{GeV}}^{-3}\;\text{GeV}^{-1}\text{sr}^{-1}\text{cm}^{-2}\text{s}^{-1}, & E_p \geqslant 5\cdot 10^6\,\text{GeV} \end{cases} \tag{2.1.18}$$

with atmospheric particles. If having significantly large lifetimes, produced HNLs may enter the detector volume of neutrino telescopes, such as IceCube and KM3NeT, located deep in ice and the Mediterranean Sea correspondingly, and decay there.

In order to probe the parameter space of HNLs, it is necessary to distinguish their decays from interactions of SM particles that are also produced in the atmosphere: neutrinos and

muons. IceCube and KM3NeT may only distinguish two event types: track-like, which corresponds to muons penetrating through the detector volume, and cascade-like, which originates from other particles such as electrons and hadrons. Scatterings of neutrinos inside the detector volume produce cascade-like (if no high-energy muons are produced) or combined cascade-like + track-like signature (if high-energy muons are produced), while penetrating atmospheric muons give rise to track-like signature.

A possible way to distinguish the SM particles events from HNLs is to look for the HNL decays into a di-muon pair, $N \to \mu\bar{\mu}\nu_\tau$. They produce a signature of two tracks originated from one point inside the detector volume, which differs from the SM events signatures.

Detectors of KM3NeT have energy and angular resolution sufficient precise for resolving the two tracks down to energies of a few tens of $10\,\mathrm{GeV}$ [73] (and much better than those at IceCube). On the other hand, characteristic energies of HNLs are $E_N \simeq 100$ GeV. Therefore, we believe that the dimuon signature may be reconstructed in the background free regime with high efficiency.[3]

2.1.5.1 Analytic estimates: comparison with CHARM

Now, let us discuss the sensitivity of KM3NeT to HNLs. We will first compare the amount of HNL decay events at CHARM and KM3NeT for the given value of the mixing angle at the lower bound of the sensitivity using simple analytic estimates. According to Eq. (2.1.8), for the ratio of decay events at these experiments we have

$$\frac{N^{(\tau)}_{\text{events,CHARM}}}{N^{(\tau)}_{\text{events,KM3NeT}}} \simeq \frac{N^{\text{CHARM}}_{c\bar{c}} \cdot \epsilon^{\text{CHARM}}_{\text{geom}} \cdot \epsilon^{\text{CHARM}}_{\text{decay}}}{N^{\text{KM3NeT}}_{c\bar{c}}} \times \frac{l^{\text{CHARM}}_{\text{fid}}}{l^{\text{KM3NeT}}_{\text{fid}}} \times \\ \times \frac{\gamma^{\text{KM3NeT}}_N}{\gamma^{\text{CHARM}}_N} \times \frac{\sum_{l=e,\mu}\Gamma(N_\tau \to ll)\epsilon_{\text{det},ll}}{\Gamma(N_\tau \to \mu\mu)} \quad (2.1.19)$$

Here, $N^{\text{CHARM}}_{c\bar{c}} \cdot \epsilon^{\text{CHARM}}_{\text{geom}} \cdot \epsilon^{\text{CHARM}}_{\text{decay}} \simeq 2 \cdot 10^{13}$ (see Fig. 2.27 is the number of $c\bar{c}$ pairs detectable fraction of HNL decay events at CHARM. $N^{\text{KM3NeT}}_{c\bar{c}}$ is the amount of $c\bar{c}$ pairs produced in the upper hemisphere propagating to KM3NeT,

$$N^{\text{KM3NeT}}_{c\bar{c}} \simeq 2\pi \times 1\ \text{km}^2 \times 5\ \text{years} \times \int \frac{d\Phi}{d\Omega dt dS dE_p} \cdot \frac{\sigma_{pp\to c\bar{c}X}}{\sigma_{pp,\text{total}}} dE_p \simeq 10^{12}, \quad (2.1.20)$$

where $\sigma_{pp\to c\bar{c}X}(E_p)$ is the energy-dependent charm production cross-section which we use from FONLL [43] and from [8], and $\sigma_{pp,\text{total}}$ is the total pp-cross-section, which we use

[3] The possible background is combinatorial and originates from pairs of oppositely charged atmospheric muons. However, it may be reduced to some extent by imposing veto on muons coming from the outer layer of the detector volume.

from [82]. The integrand in (2.1.20) is the product of two competing factors: $\frac{d\Phi}{d\Omega dt dS dE_p}$, which decreases with the proton's energy, and $\sigma_{pp\to c\bar{c}X}(E_p)$, which increases, see Fig. 2.7.

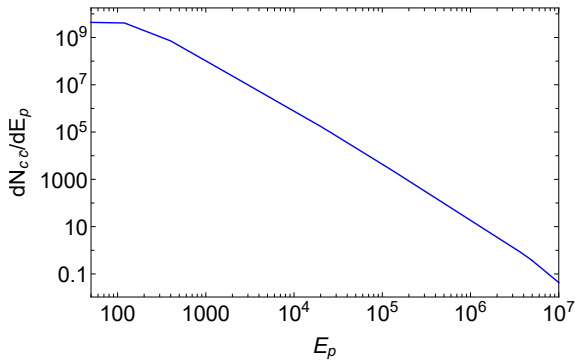

Figure 2.7: The integrand of Eq. (2.1.20).

We approximate the ratio of the mean HNL γ factors by the ratio of the mean γ factors of D mesons:

$$\gamma_N^{\text{KM3NeT}}/\gamma_{D_s}^{\text{CHARM}} \simeq \gamma_{D_s}^{\text{KM3NeT}}/\gamma_{D_s}^{\text{CHARM}} \simeq 3, \tag{2.1.21}$$

where we calculate $\gamma_{D_s}^{\text{KM3NeT}}$ using the $c\bar{c}$ distribution $\frac{d\Phi}{d\Omega dt dS dE_p} \cdot \sigma_{pp\to c\bar{c}X}$, assuming that $E_D \approx E_p/2$.

Using the fiducial lengths $l_{\text{fid}}^{\text{CHARM}} = 35\,\text{m}$ and $l_{\text{fid}}^{\text{KM3NeT}} \simeq 1\,\text{km}$, and taking into account that the last factor in Eq. (2.1.19) is $\mathcal{O}(1)$ for $m_N \gg 2m_\mu$, we finally obtain

$$\frac{N_{\text{events,CHARM}}^{(\tau)}}{N_{\text{events,KM3NeT}}^{(\tau)}} \simeq 2 \tag{2.1.22}$$

Using the analytic estimates, we conclude that even in the most optimistic case (assuming unit efficiency) the number of events at CHARM and KM3NeT are just comparable. We need more accurate estimate taking into account non-isotropic distribution of the produced HNLs.

2.1.5.2 Accurate estimate

We compute the production of D_s mesons (and hence τ leptons) using the approach from [81]. The production was found to be maximal at $O(10\,\text{km})$ height from the Earth's surface. The resulting spectrum $\frac{d\Phi_{D_s}}{dS dt dl d\cos(\theta) dE_{D_s}}$ of D_s mesons is in good agreement with Fig. 2 from [83]. The total number of D_s mesons produced in the direction of KM3NeT during the operating time 5 years was found to be $N_{D_s} \simeq 5 \cdot 10^{10}$.

Next, we use the approach from [83] in order to estimate the sensitivity of KM3NeT.

The number of decay events is

$$N_{\text{events}} \approx S_{\text{Km3NeT}} \times T \times \int \frac{d\Phi_{D_s}}{dS dt dl d\cos(\theta) dE_{D_s}} \cdot \text{Br}(D_s \to \tau \bar{\nu}_\tau) \cdot \\ \cdot \text{Br}(\tau \to N_\tau X) \cdot P_{\text{decay}}(l, E_N) d\cos(\theta) dl dE_N, \quad (2.1.23)$$

where $T = 5$ years is the operating time, $S_{\text{KM3NeT}} = 1\,\text{km}^2$ is the transverse area of KM3NeT. The decay probability is

$$P_{\text{decay}} \approx e^{-(l+l_1)/l_{\text{decay}}} - e^{-(l+l_2)/l_{\text{decay}}}, \quad (2.1.24)$$

where l is the distance from the HNL production point in atmosphere, $l_1 \approx 3\,\text{km}$ is the distance from the surface of Earth to the KM3NeT detector, while $l_2 = l_1 + 1\,\text{km}$ is the distance to the end of the KM3NeT. For simplicity, in l_{decay} we set $E_N \approx E_{D_s}/2$. In order to show the maximal reach of KM3NeT, we optimistically assume unit efficiency of the dimuon event reconstruction, and require $N_{\text{events}} > 3$ during the operating period.

The resulting sensitivity shown in Fig. 2.6 is worse than predicted by the simple estimate by a factor of few. The reason is that at masses $m_N \lesssim 500\,\text{MeV}$ there is an additional suppression from $\text{Br}(N \to \mu\mu)$, while at higher masses the scaling (2.1.8) is not valid because the lower bound is close to the upper bound.

2.2 Searches with displaced vertices at the LHC

A peculiar feature of dedicated beam experiments such as SHiP, DUNE, and MATHUSLA is that they have macroscopic distance from the collision point $l_{\text{min}} \gg 1$ m to the detector volume. On one hand, it allows to reduce background from SM particles down to controllable and even negligible level. On the other hand, such experiments cannot search for short-lived FIPs with decay lengths $c\tau\gamma \ll l_{\text{min}}$.

> Because of macroscopic distance from the FIP production point and the detector volume at Intensity Frontier experiments, there is a domain of large couplings that is neither excluded by past experiments nor may be probed by dedicated beam experiments, see Fig. 2.8.

To probe such intermediate couplings, one needs experiments that have much shorter l_{min}, and simultaneously may handle the background coming from SM events, the amount of which increases if decreasing l_{min}. Such type of experiments exists at the LHC and is called **displaced vertices scheme** (DV).

An event at a given DV experiment has to meet some selection criteria which are specific to the experiment, minimize the SM background yield and simultaneously should not diminish the detected amount of events with FIPs. The physical process involving

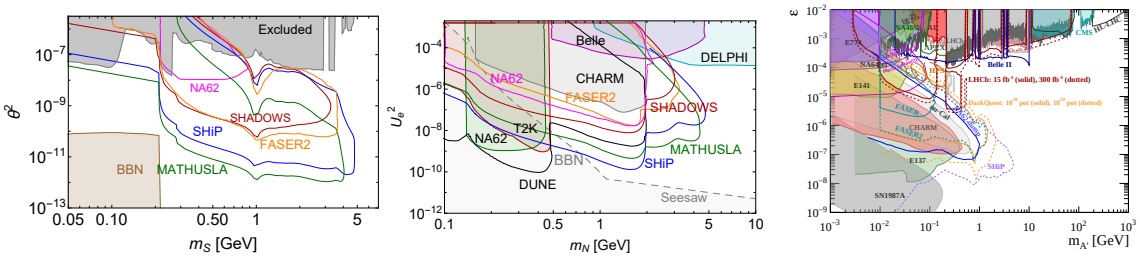

Figure 2.8: Sensitivity reach of Intensity Frontier experiment to decays of portal particles: dark scalars (1.1.1) that have zero quartic coupling $HHSS$ (the left panel), Heavy Neutral Leptons (1.1.2) that mix purely with ν_e (the middle panel), and dark photons (1.1.3) (the right panel). For the description of the lines, see Fig. 1.2. For all of the models, there is a gap between the domain that may probed by Intensity Frontier experiments and the parameter space closed by past experiments, which is due to finite distance from FIPs production point to the decay volume of Intensity Frontier experiments.

FIP consists of the production vertex (PV, in which a FIP is produced) and the displaced decay vertex, in which it decays, see Fig. 2.9; an important selection criterion is whether the requirement of the PV to be tagged in addition to the reconstruction of the DV. The tagging is done with a help of a prompt decay product such as a lepton or a jet. Currently, the PV tagging is essential to have a DV event triggering, so that it is recorded and can be analyzed offline. This type of searches is already performed at ATLAS, CMS and LHCb, see e.g. [84–89]. The second type of schemes does not require such tagging. It will be available after the phase II upgrade, during the high-luminosity LHC phase, when the possibility to use track-trigger in CMS will be introduced. This will enable a possibility to reconstruct and identify displaced tracks online [90–92], and hence will remove a need for a prompt product in the event. Estimates of the sensitivity of one of such schemes which utilizes the L1 trigger at CMS may be found e.g. in [93].

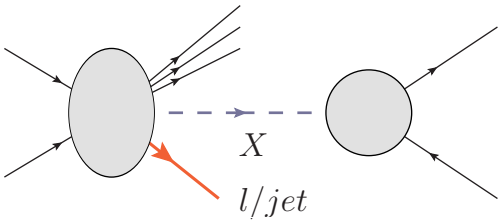

Figure 2.9: Schematic diagram of searches for FIPs with displaced vertices schemes at the LHC. A FIP X produced at the production vertex (PV) travels a macroscopic distance and then gives rise to a displaced decay vertex (DV). Displaced vertices schemes that are currently available require tagging of the PV, which is typically done with the help of a lepton or jet produced in the PV (shown in red). During Run 4, schemes that do not require such tagging will be available.

ATLAS, CMS and LHCb experiments complement each other in searches for FIPs: LHCb covers mass range $m_{\rm FIP} \lesssim m_B$, while ATLAS/CMS allow for searching in the range $m_B \lesssim m_{\rm FIP} \lesssim m_h$.

Indeed, the flux of SM particles that may produce FIPs (such as W/Z bosons, the Higgs boson, and B, D mesons) is collimated with respect to the beam axis.[4] Naively, one may expect that the best placement of a DV experiment is in the forward region that covers relatively small angles. However, decay products of these particles gain characteristic transverse momentum of order of $p_T \simeq m_{\rm mother}$, where $m_{\rm mother}$ is the mass of decaying particle. For large enough $m_{\rm mother}$ (for instance, for Higgs bosons), the characteristic angle $\theta \simeq \arctan(p_T/p_L)$ becomes much larger than the angular width of the mother particle distribution. Then, instead of the forward region, the preferable setup is the one covering large angular domain. ATLAS and CMS are located off-axis and have significant angular coverage, thus allow us to search for FIPs produced in decays of heavy particles such as the Higgs boson and W/Z bosons. LHCb, in its turn, covers much smaller angular domain but in the forward region, and thus allow to search for FIPs originating from decays of relatively light B mesons, for which the broadening is insignificant.

In this section, we discuss the potential for the search scheme at CMS that utilizes muon trackers. Advantages of this scheme is large length of the decay volume, which is essential to probe the parameter space of the LLPs with the decay lengths about 1 meter or larger, and relatively small background as compared to the schemes that search for hadronic decays. We use Heavy Neutral Leptons, Chern-Simons portal and dark scalars as three examples of long-lived particles for which the CMS muon tracker can provide essential information about their properties.

2.2.1 Displaced vertices with muon tracker at CMS

Typically, DV search schemes use inner trackers to reconstruct events. Therefore, the maximal displacement that may be reconstructed is limited by $\mathcal{O}(0.5\ \text{m})$. Alternatively, one may use muon chambers, that cover much larger distance (up to 3 m in the transverse plane at CMS).

The use of the muon chambers to reconstruct di-muon DV signatures has been explored in the past in [94–96] and recently in [97]. Ref. [98] that appeared when this work was at its final stage employed the event selection criteria that may be too optimistic with regard to the background estimates. Ref. [99] explored a potential of the CMS muon chambers *alone* to reconstruct dimuon DV. This search however, was constructed to be much more

[4] For instance, the angular distribution of B mesons and the Higgs bosons quickly drops at angles $\theta > 0.01$ rad.

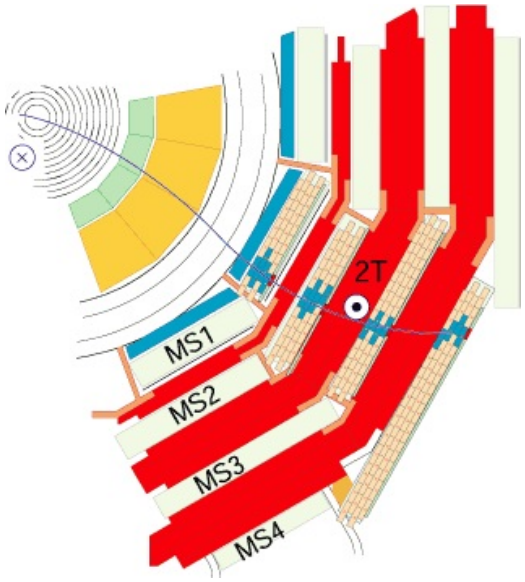

Figure 2.10: Cross-section of the CMS experiment. Layers (muon stations) of the muon detector in the plane perpendicular to the beam direction. The figure is from [103].

general, and hence could not profit from the presence of a prompt lepton in the event. This necessarily implied much more stringent cuts on p_T of either of the two muons in the muon tracker since these muons were used to record an event by a trigger, and therefore lower sensitivity.

2.2.1.1 Description of the scheme

CMS (compact muon solenoid) is a beam line azimuthally symmetric detector consisting of a solenoid generating the 3.8 T magnetic field, the inner trackers that allow to reconstruct the momentum of particles produced in the pseudorapidity range $|\eta| < 2.5$ (where $\eta = -\log[\tan(\theta/2)]$ and θ is the polar angle with respect to the anticlockwise-beam direction) and the muon trackers located outside the solenoid [100].

The muon system is located outside the solenoid and covers the range $|\eta| < 2.4$. It is a set of gaseous detectors sandwiched among the layers of the steel flux-return yoke. This allows for a muon to be detected along the track path at multiple points [101]. The magnetic field in the muon system is not uniform, and goes from 2 T in the innermost part down to almost 0 T in the outer part [102]. Schematic drawing of the muon detector is shown in Fig. 2.10.

For the LHC Run 2, new reconstruction of muons has been introduced [104], the so-called displaced standalone muon reconstruction. This reconstruction is specifically designed to address cases when muons are produced in decays far away from the production vertex. New algorithm achieves an almost 100% reconstruction efficiency for the muon production radius up to about 3 m. This is a significant gain in the efficiency compared to the reconstruction which uses also inner tracker information, but at the same time, the

momentum resolution deteriorates by about a factor of 10 and is in the range 10–60%.

The muon tracker can use two muon tracks to reconstruct a displaced vertex originating from the decay $X \to \mu\mu + \ldots$. The reconstructed DV together with the production vertex that can be tagged by prompt decays products, *e.g.* a prompt lepton, and an underlying event produced together with the X particle, is identified as a DV event. Due to the large distance between a PV and a reconstructed DV, we will call this scheme the "the long DV" scheme.

It should be noticed, that after the phase II upgrade, during the high-luminosity LHC phase, the possibility to use track-trigger in CMS will be introduced. This will enable a possibility to reconstruct and identify displaced tracks online [90–92], and hence will remove a need for a prompt lepton in the event. However, for the models discussed in this paper, current hardware configuration of the CMS allows to perform the searches with the already recorded data, as well with the data to be obtained during the Run 3 of the LHC.

At the same time, final states with a prompt, well identified, object in the event, as *e.g.* a prompt muon or electron, have much lower background rate. In this case the instrumental backgrounds and non-muon backgrounds from cosmic rays are reduced to a negligible level. The remaining cosmic-ray muon backgrounds can be suppressed by selections which do not impact signal efficiency, as described in Ref. [105]. The remaining sources of the background for the long DV scheme are processes with a presence of a prompt object (as e.g. W boson production) accompanied by decays of the SM particles into single muons, which give rise to combinatorial two-muon events, and two-muon decays of the SM particles (for example, $J/\psi, \rho, \omega$ mesons and the Z boson). The most significant displacement of such DV appears in case of two muons originating for a heavy-flavor particle decay (b or c hadrons). As we do not carry out an experimental analysis in this paper, we assume that this background is negligible if one requires the transverse position of the displaced vertex to be as far as $l_{\text{DV}} > 2$ cm from the beam collision point, since most of the SM particles decay before reaching this displacement [106]. Under this assumption we lose a part of the efficiency for LLPs with shorter lifetimes, but at the same time we provide a more robust estimate of the potential signal sensitivity. Because of the position of the muon trackers, the muon events can be reconstructed at the distances $l_{\text{DV}} < 3$ m. The muons can be reconstructed with high efficiency and low misidentification probability if each of them has the transverse momentum $p_T > 5$ GeV [107, 108].

To summarize, an event in the long DV search scheme should satisfy the following selection criteria:

- A prompt electron with $|\eta| < 2.5,\ p_T > 30$ GeV or a prompt muon with $|\eta| < 2.4,\ p_T > 25$ GeV, which are required for an event to be recorded by the single lepton triggers;
- The minimal transverse displacement of the DV from the PV is $l_{\text{min},\perp} = 2$ cm; the maximal transverse and longitudinal displacements are $l_{\text{max},\perp} = 3$ m, $l_{\text{max},l} = 7$ m;

– Two displaced muon tracks, each with $|\eta| < 2.4,\ p_T > 5$ GeV.

The requirement of a large displacement of a DV from the PV helps to significantly reduce the background from SM processes. Therefore, even in the region with the invariant mass of two muons below 5 GeV (mass of B-mesons) the SM background is considered to be negligible. The scheme is presented in Fig. 2.11.

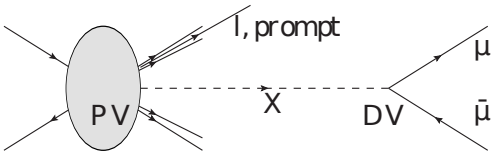

Figure 2.11: Schematic diagram of the search scheme of LLPs at CMS using the muon detectors. The production vertex (PV) is tagged by the prompt lepton l, while the displaced vertex (DV) is reconstructed by two muons produced in the decay $X \to \mu\mu$.

An event with prompt τ lepton can be tagged by its leptonic decays $\tau \to l\bar{\nu}_l\nu_\tau$, where the leptons $l = e/\mu$ satisfy the criteria for prompt leptons presented above. We do not consider the reconstruction of τ leptons by their hadronic decay products since the trigger threshold for p_T of hadronic decay products is too high for efficient reconstruction.[5] However, in the future it is wise to invest into the development of a dedicated multi-object trigger which would allow to bring down the prompt tau p_T by including additional displaced leptons in the event.

In [98] a similar search scheme was discussed, albeit with less restrictive selection criteria $l_{\text{min},\perp} = 0.5\,\text{cm}$, $l_{\text{max},\perp} = 4\,\text{m}$, and $|\eta| < 4$ for leptons.[6] A wider range of muon pseudorapidities leads to the enlargement of the selection efficiency, while a smaller displacement between a DV and the PV lifts up the upper bound of the sensitivity and hence increases the maximal mass reach. However, we caution that the background-free hypothesis for the region with smaller DV displacements adopted in [98] has not been tested. Nevertheless, to demonstrate potential improvement from considering lower displacements we provide sensitivity for two scenarios: "realistic" for the selection criteria outlined above, and "optimistic", defined according to [98].

2.2.1.2 Estimation of the number of events

The number of decay events of a new particle X that pass the selection criteria is

$$N_{\text{events}} = N_{\text{parent}} \cdot \text{Br}_{\text{prod}} \cdot P_{\text{decay}} \cdot \epsilon, \tag{2.2.1}$$

where

[5] Current trigger threshold is $p_T > 180$ GeV.

[6] After the HL-LHC upgrade the CMS will extend its pseudorapidity range to $|\eta| < 4$.

– N_{parent} is the total number of parent particles that produce a particle X at the LHC;
– Br_{prod} is the branching fraction of the production of a particle X in decays of the parent particle;
– P_{decay} is the decay probability,

$$P_{\text{decay}} = \int d\theta_X dp_X f(p_X, \theta_X) \times \left(e^{-l_{\min}/c\tau_X\gamma_X} - e^{-l_{\max}/c\tau_X\gamma_X}\right), \quad (2.2.2)$$

with τ_X being the proper lifetime of the particle X, γ_X is its γ factor, and $f(p_X, \gamma_X)$ is the distribution function of the X particle whose decay products satisfy the selection criteria;
– ϵ is the *overall efficiency* – the fraction of all decays of the X particle that occurred in the decay volume between $l_{\min}$ and $l_{\max}$, have passed the selection criteria, and were successfully reconstructed.

The efficiency is a combination of several factors:

$$\epsilon = \epsilon_{\text{sel}} \cdot \epsilon_{\text{rec}} \cdot \text{Br}_{X\to\mu\mu}, \quad (2.2.3)$$

where $\epsilon_{\text{sel}}, \epsilon_{\text{rec}}$ are the efficiencies of the selection and subsequent reconstruction of an event correspondingly, and $\text{Br}_{X\to\mu\mu}$ is the branching ratio of the decay of the X particle into two muons. Clearly, ϵ_{rec} does not depend on the nature of LLP. The reconstruction efficiency for leptons is well above 95% for muons with $p_T > 5$ GeV [101, 104, 107] and for electrons with $p_T > 30$ GeV [109]. Therefore, for simplicity the reconstruction efficiency is taken to be equal to 1 ($\epsilon_{\text{rec}} = 1$) in what follows.

We define the sensitivity curves by the condition $N_{\text{events}} \simeq 3$, corresponding to the 95% exclusion limit under the assumption of zero background. The lower boundary can be easily rescaled to other N_{events}.

The main advantage of the long DV scheme is the large length of the fiducial decay volume $l_{\max}$, which exceeds the lengths of the decay volumes of other DV search schemes at the LHC (see, e.g., [85, 110]) by $\simeq 10$ times. This has a benefit when searching for new particle with large decay lengths,

$$l_{\text{decay}} \equiv c\tau_X\gamma_X \gg l_{\max} \quad (2.2.4)$$

Indeed, in this case the decay probability (2.2.2) is in the "linear regime", $P_{\text{decay}} \approx l_{\max}/l_{\text{decay}}$, and as a result the number of events (2.2.1) is proportional to $l_{\max}$. For decay lengths that do not satisfy the condition (2.2.4) the decay probability does not depend on $l_{\max}$, and the improvement is lost (see Fig. 2.12).

In order to probe the domain (2.2.4) there must be sufficient production of the X particles, i.e.

$$N_{\text{prod}} \cdot \text{Br}_{X\to\mu\mu} > 3, \quad (2.2.5)$$

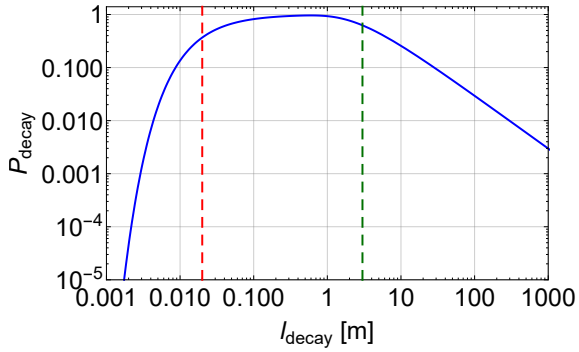

Figure 2.12: Dependence of the decay probability (2.2.2) on the decay length l_{decay}. For simplicity we assumed that all the particles travel with the same momentum and in the same direction, and set $l_{\text{max}} = 3$ m. The dashed lines denote the values $l_{\text{decay}} = l_{\text{min}}$ and $l_{\text{decay}} = l_{\text{max}}$. In the domain $l_{\text{decay}} \gg l_{\text{max}}$ the decay probability scales as $P_{\text{decay}} \simeq l_{\text{max}}/l_{\text{decay}}$, while in the domain $l_{\text{min}} \lesssim l_{\text{decay}} \lesssim l_{\text{max}}$ it behaves approximately constantly and does not depend on l_{max}.

where $N_{\text{prod}} = N_{\text{parent}} \cdot \text{Br}_{\text{prod}}$. The parameter space defined by the conditions (2.2.4), (2.2.5) is optimal for being probed by the long DV scheme. A toy example of the parameter space is given in Fig. 2.13.

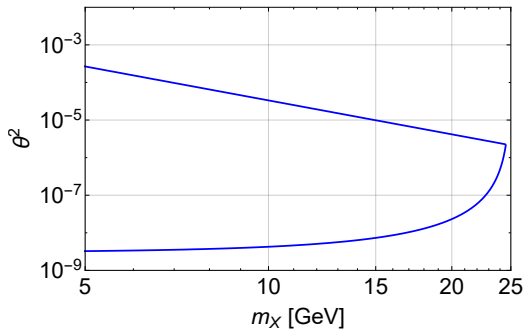

Figure 2.13: The illustration of the parameter space which is optimal for being probed with the long DV scheme, see text for details. We used a toy model with $N_{\text{prod}} = 10^9 \left[1 - m_X^2/(25\text{ GeV})^2\right]^2 \theta_X^2$, $\text{Br}_{X\to\mu\mu} = 1$ and $l_{\text{decay}} = 0.1 m_X^{-3} \theta_X^{-2}$ m.

2.2.1.3 HNLs

We start with HNLs. The main production channel of the HNLs with masses in the range $m_N \gtrsim 5$ GeV is the decay of the W bosons. We use the value $\sigma_W \approx 190$ nb for the total production cross section of the W bosons at the LHC at energies $\sqrt{s} = 13$ TeV [111]. To estimate the parameter space defined by (2.2.4) and (2.2.5), we calculated the energy spectrum and geometric acceptance ϵ_{geom} of the HNLs in the pseudorapidity range $|\eta| < 2.5$ in LO using the model *HeavyN* [112]. We found $\epsilon_{\text{geom}} \approx 0.5$ for the mass range $m_N \lesssim 20$ GeV and $E_N \approx 80$ GeV.

ϵ_{sel}	e	μ	τ
Realistic	0.16	0.17	$7 \cdot 10^{-3}$
Optimistic	0.26	0.31	$3.2 \cdot 10^{-2}$

Table 2.2: The values of the selection efficiencies for HNLs of different flavors e, μ, τ in the case of realistic and optimistic selection criteria

In Fig. 2.14, we show the parameter space for the HNLs mixing with ν_μ that can be optimally probed by the long DV scheme. We see that the domain where the long DV

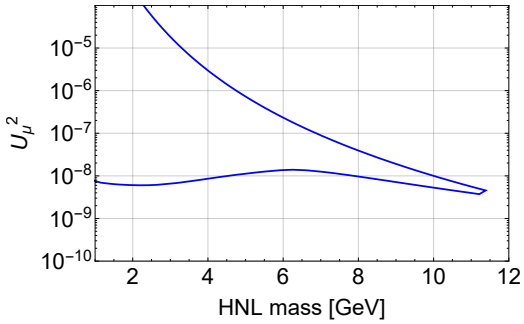

Figure 2.14: The parameters of HNLs mixing with ν_μ that satisfy criteria (2.2.4) –(2.2.5) for the LHC luminosity $\mathcal{L} = 3000$ fb^{-1}. Note, this is *not* an exclusion region, see text around equations for details.

scheme has good potential corresponds to the masses $m_N < 10$ GeV and the mixing angles $U^2 \gtrsim 10^{-9}$.

Simulations. To find the efficiency for the HNLs mixing with $\nu_{e/\mu}$, we used MadGraph5 [113] with the model *HeavyN* [112]. For simulating decays of τ lepton, we used *taudecay_UFO* model [114]. For the mixing with $\nu_{e/\mu}$ we simulated the process $p+p \to W,\ W \to l+N$, where $l = e$ for the mixing with ν_e and $l = \mu$ for the mixing with ν_μ, with subsequent decay $N \to \mu^+ + \mu^- + \nu/\bar{\nu}_l$. In the case of the mixing with ν_τ, we simulated the process $p+p \to W, W \to \tau + N$ with subsequent decays $N \to \mu^+ + \mu^- + \nu_\tau/\bar{\nu}_\tau$ and $\tau \to l + \bar{\nu}_l + \nu_\tau$, where $l = e/\mu$.

Using the selection criteria for the long DV scheme, we computed the selection efficiencies. They were found to be almost independent of the mass of the HNL in the mass range 1 GeV $< m_N <$ 20 GeV. We give their values in Table 2.2. The suppression of the efficiency for mixing with ν_τ is due mainly to the reconstruction of the prompt τ event. Indeed, the amount of the leptons produced in the decay $\tau \to l\bar{\nu}_l\nu_\tau$ and passing the p_T selection criterion for the prompt leptons is ≈ 0.1.

For the average momentum we found $p_N \approx 70$ GeV and $p_N \approx 180$ GeV for the realistic and optimistic estimates correspondingly.

Comparison with other schemes. Let us compare the sensitivity of the long DV search scheme to the HNLs with a scheme from [110, 115] that uses inner trackers at ATLAS to search for DVs events (c.f. [97]). Owing to its smaller transverse displacement

$l_{\max} = 0.3$ m we call it the "*short DV scheme*". For the estimation of the sensitivity of the short DV scheme we use parameterized efficiencies $\epsilon(m_N, U^2)$ provided by the authors of [110]. The comparison of the sensitivities is given in Fig. 2.15. We show both optimistic and realistic estimate of the sensitivity of the long DV scheme. We also show the sensitivity of the SHiP experiment from [80] that serves for an illustration of the sensitivity reach of Intensity Frontier experiments.

The long DV scheme allows to search for HNLs in the unexplored region of the parameter space that is not accessible to other Intensity Frontier experiments or other LHC searches. Its difference in the sensitivity with the short DV scheme is due to three reasons. First, for masses $m_N \lesssim 10$ GeV the decay probability for both the schemes is in the linear regime (see Sec. 2.2.1.2), and therefore the long DV scheme gets the benefit from the 10 times larger length of the decay volume $l_{\max}$. Second, for the masses 5 GeV $\lesssim m_N \lesssim 10$ GeV there is a drop of the overall efficiency for the short DV scheme. This is caused by the selection criteria on the reconstructed invariant mass of the DV, $m_{\text{DV}} > 5$ GeV, and the charged tracks, $N_{\text{trk}} \geqslant 4$, that are needed to remain in the background free region [87]. Third, because of absence of the hadronic background the long DV scheme can probe the parameter space $m_N \lesssim 5$ GeV, which is not reachable by the short DV scheme.

Nevertheless, both the schemes are complementary to each other and provide a cross-check in the mass region 5 GeV $< m_N < 15$ GeV.

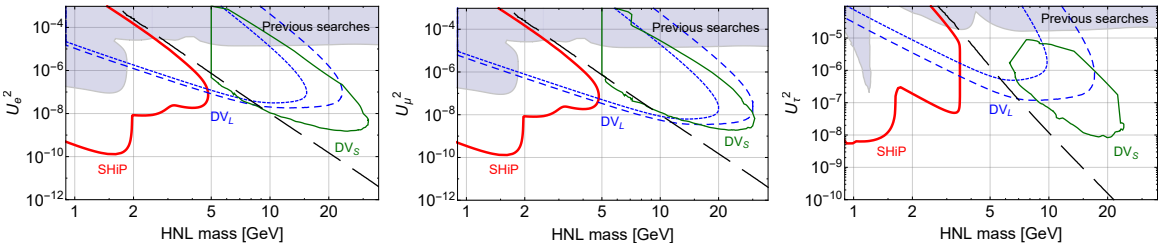

Figure 2.15: The sensitivity of the long DV (DV_L) and short DV (DV_S) search schemes to HNLs mixing with ν_e (upper panel), ν_μ (middle panel) and ν_τ (lower panel). By the blue short dashed line we denote the realistic sensitivity obtained using the selection criteria presented in this paper, while the blue dashed line corresponds to the optimistic estimate of the sensitivity using relaxed selection criteria from [98], see Sec. 2.2.1.2 for details. The sensitivity of the SHiP experiment is taken from [80]. Black long-dashed line indicates HNL parameters that correspond to $l_{\text{decay}} = 3$ m. The estimates are for the high luminosity LHC phase, $\mathcal{L} = 3000$ fb^{-1}. For the DV search schemes sensitivity we require $N_{\text{events}} \geq 3$ and assume zero background (see text for details).

2.2.1.4 Chern-Simons portal

Chern-Simons portal introduces a vector particle X interacting with pseudo-Chern-Simons current of the SM gauge bosons [82, 116]:

$$\mathcal{L}_{CS} = c_W \epsilon^{\mu\nu\lambda\rho} X_\mu W_\nu \partial_\lambda W_\rho + \\ c_\gamma \cos\theta_W \epsilon^{\mu\nu\lambda\rho} X_\mu Z_\nu \partial_\lambda \gamma_\rho + c_Z \sin\theta_W \epsilon^{\mu\nu\lambda\rho} X_\mu Z_\nu \partial_\lambda Z_\rho \quad (2.2.6)$$

We can add the interaction of the X boson with SM leptons in the form

$$\mathcal{L}_{X\mu\mu} = c_W g_{Xll} X^\nu \sum_{l=e,\mu,\tau} \bar{l}\gamma_5\gamma_\nu l, \quad (2.2.7)$$

where g_{Xll} is a dimensionless constant.[7]

Let us consider the case when $c_\gamma, c_Z \ll c_W$. Then the production of the X particle in pp collisions goes through the XWW vertex, while the decay goes through the vertex (2.2.7) down to very small couplings $g^2_{Xll} \simeq 10^{-7}$ for the X bosons as heavy as $m_X \simeq 40$ GeV, see Appendix 2.2.1.4. These vertices are parametrically independent, and for particular values of g_{Xll} it is possible to probe the parameter space in the optimal domain for the long DV scheme. The process of interest is

$$W \to X + l + \bar{\nu}_l, \quad X \to \mu^+ + \mu^- \quad (2.2.8)$$

The lepton l produced in the W decay can be triggered as a prompt lepton, while the muon pair from the decay of the X boson can be reconstructed as displaced muons, which meets the selection criteria of a DV event within the long DV scheme.

To find the selection efficiency and the energy spectrum of the W bosons, we implemented the model of the X boson (2.2.6), (2.2.7) into the MadGraph using FeynRules [117, 118]. The model is publicly available [119]. We simulated the processes $p+p \to e^+/\mu^+ + \nu_{e/\mu} + X$ (plus the charge conjugated final states) with subsequent decays $X \to \mu^+\mu^-$. We have found that the overall efficiency is $\epsilon \approx 2.3 \cdot 10^{-2}$ for m_X ranging from 1 GeV to 20 GeV. The average momentum of the X boson $p_X \approx 40$ GeV.

The sensitivity to the Chern-Simons portal is shown in Fig. 2.16. We conclude that the long DV scheme can probe masses up to $m_X \simeq 30$ GeV and couplings down to $c^2_W \simeq 10^{-9}$. We note that the probed parameter space is well below the current experimental bound on c_W, which is $c^2_W \lesssim 10^{-3}(m_X/1\text{ GeV})^2$ [82].

[7] The coupling g_{Xll} can be generated effectively by the interaction (2.2.6) or be an effect of new physics.

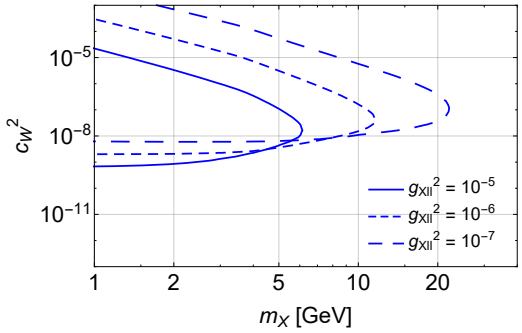

Figure 2.16: The sensitivity of the long DV scheme at the high luminosity phase to the Chern-Simons portal for different values of the coupling to muons (2.2.7). For the DV search schemes sensitivity we require $N_{\text{events}} \geq 3$ and assume zero background (see text for details).

2.2.1.5 Dark scalars with quartic coupling

In the case of dark scalars with quartic coupling (remind Eq. (1.1.1)) and masses $m_S > m_B$, the production and decay channels are independent of each other [120], similarly to the case of Chern-Simons portal.

Namely, the production occurs via the quartic coupling – it is a decay of Higgs bosons $h \to SS$, while decays are mediated by the mixing angle [38]. The branching ratio of

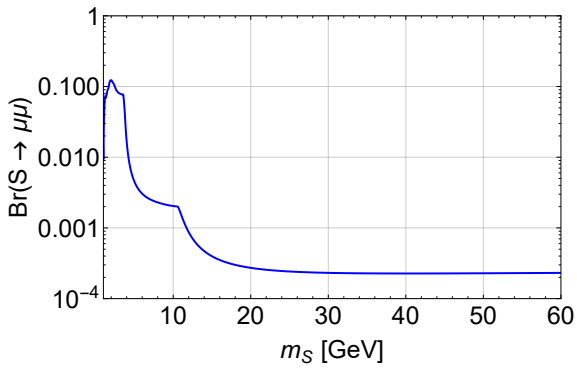

Figure 2.17: The branching ratio of decays of scalars into two muons. It does not include muons produced as secondary particles from decays of heavier decay products, whose contribution may dominate at larger masses.

decays of scalars into two muons is shown in Fig. 2.17. The interaction of scalars with fermions is similar to the interaction of Higgs bosons. Therefore, above scalar masses $m_S \simeq 2m_\pi$, it is strongly suppressed because of the Yukawa couplings. Nevertheless, despite the suppression of the signal yield by small $\text{Br}(S \to \mu\mu)$ it is still possible to search for heavy scalars using the muon trackers. In addition, as in Fig. 2.17 we do not include pair

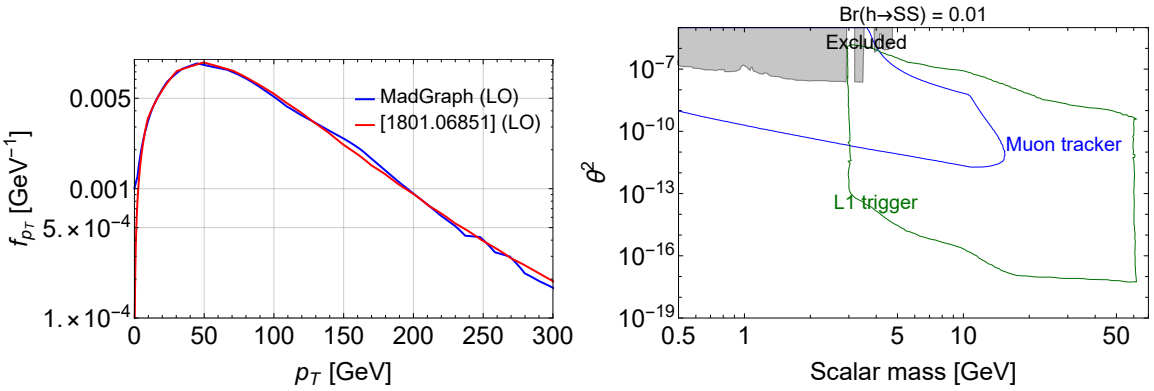

Figure 2.18: *Left panel*: The p_T spectrum of Higgs bosons produced in the process $p+p \to h+W^+,\ W^+ \to l^+ + \nu_l$ obtained in our simulations using MadGraph (blue) and in [121] for the selection criteria $|\eta_l| < 2.5$, $p_{T,l} > 15$ GeV. *Right panel*: the sensitivity of the muon tracker DV scheme to scalars, assuming the production branching ratio $\text{Br}(h \to SS) = 0.01$. In green, we also show the sensitivity of the search scheme that uses L1 trigger from [122], assuming zero background.

of muons from decays of heavier decay products of scalars, our estimate of the sensitivity is conservative.

Unlike HNLs and Chern-Simons portal mediator, the main production channel of scalars, $h \to SS$, does not include a lepton, and naively it is impossible to tag the production vertex. However, one may use leptons produced together with Higgs bosons in a process

$$p+p \to h+W/Z, \quad W/Z \to l+X, \quad h \to S+S \tag{2.2.9}$$

Indeed, h, W, Z bosons have extremely small lifetimes, and all the processes (2.2.9) occur practically at one point. The process (2.2.9) is $\simeq 50$ times less frequent than the main production channel of the Higgs boson – the gluon fusion.

Simulation. In order to simulate events of scalar decays, we have first implemented the model of a scalar into MadGraph using FeynRules. Next, we have simulated the chain (2.2.9) at LO, together with further scalar decays. NLO corrections to the spectra are known to be negligibly small [121]. To validate our simulations for the production of Higgs bosons and leptons in this process, we compare of the p_T spectrum of Higgs bosons produced in the process $p+p \to h+W^+,\ W^+ \to l^+ + \nu_l$ with the spectrum from [121], see Fig. 2.18.

Sensitivity. In Fig. 2.18, we show the sensitivity to the scalar portal assuming the branching ratio $\text{Br}(h \to SS) = 0.01$, which is well below the reach of future searches for invisible decays of Higgs bosons at LHC Run 3 and at the High-Luminosity (HL) LHC (HL-

LHC, Run 4), which are projected to have sensitivity at the level $\mathrm{Br}_{h\to\mathrm{inv}} \sim 0.05$ — 0.15 at 95% CL [123] maybe going all the way to a few *percents* [124].

We also include the sensitivity of the scheme with L1 tracker at CMS [122], which does not require a prompt lepton for triggering. Together with the fact that it requires 4 charged tracks each with $p_T > 1$ GeV, and may search for decay products other than muons, this leads to significantly better sensitivity at the lower bound. However, independent observation (or non-observation) of events at this scheme and at the scheme with muon trackers would allow to measure independently branching ratios of different decay channels of scalars, and in particular to distinguish it from other models that have similar decay modes (such as an ALP with additional trilinear coupling to Higgs bosons).

2.2.1.6 Summary

In this section, we have proposed a new method of searching for long-lived particles at LHC ("*the long DV scheme*") that utilizes the muon tracker at the CMS experiment. It uses a prompt lepton and a displaced muon pair to reconstruct a displaced vertex event. The scheme is optimal for probing the parameter space of the LLPs with the decay lengths $l_{\mathrm{decay}} \gtrsim 3$ m. We demonstrated the potential of the scheme using three exemplary models: heavy neutral lepton (HNL), Chern-Simons portal, and scalars with quartic coupling. For HNLs, we made a comparison between the long DV scheme and other planned searching schemes at ATLAS/CMS, see *e.g.* [97, 110].

Our conclusions are the following:

- For the HNLs, the long DV scheme can probe the parameter space in the mass range $m_N \lesssim 20$ GeV and down to the mixing angles $U^2 \sim 10^{-8}$ (when mixing with ν_μ).
- The long DV scheme has a unique opportunity to probe the LLPs that decay predominantly into leptons, which is demonstrated by the example of the Chern-Simons portal;
- The long DV search scheme has a sufficiently low SM background even for LLPs with the masses $m \lesssim 5$ GeV, which is unavailable for DV search schemes at the LHC that look for hadronic decay products. In the case of HNLs, this gives a possibility to probe the parts of the parameter space that have not been probed by previous experiments and are outside the reach of the planned Intensity Frontier experiments.
- Although scalars have small branching ratio of decay into muons, the scheme still has potential to search for them, and may be complementary to other search schemes, e.g. those that do not require a prompt lepton for tagging.

2.3 Searches for light dark matter at SND@LHC

Historically, the first model of dark matter was WIMP (Weakly Interacting Massive Particle) – a massive electrically neutral fermion that interacts with SM particles via weak interactions. Similarly to neutrinos, WIMPs were at thermal equilibrium in the early Universe, which has maintained by processes WIMP + WIMP $\leftrightarrow$ SM + SM.

> Because of tiny interaction strength, light WIMPs may leave thermal equilibrium at high temperatures $T \simeq m_{\text{WIMP}}$, when their number density is not Boltzmann-suppressed. Therefore, their energy density would overproduce the Universe. This happens if masses are $m_{\text{WIMP}} \lesssim 5$ GeV. The corresponding bound is known as the Lee-Weinberg bound [125].

To evade the Lee-Weinberg bound, one may assume the existence of a mediator other than W, Z bosons that mediates the WIMP annihilation with larger strength. DM candidate particles in such models may be made lighter than 5 GeV and are called light dark matter (or LDM).

> In the minimal model with an LDM χ and mediator V, there are several parameters: LDM mass, mediator's mass, mediator's coupling to SM particles g, mediator's coupling to LDM g_χ. The information about these parameters may be obtained using combined results from searches by different experiments, see Sec. 1.2 and Fig. 2.19.

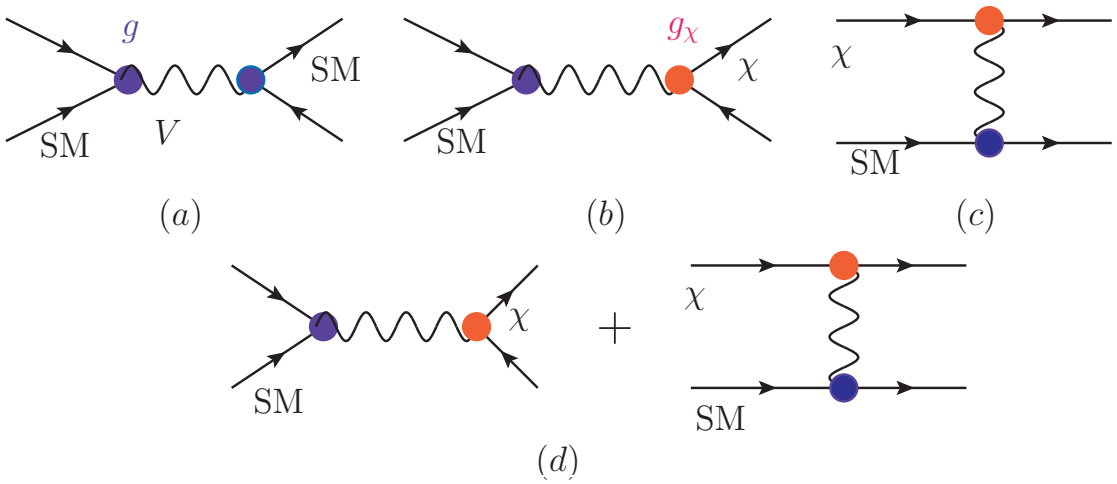

Figure 2.19: Different search schemes for LDM and mediator: visible (a) and invisible (b) decays of mediator, scatterings of LDM χ from the local DM population in our galaxy (c), and scatterings of LDM produced at accelerator experiments (d).

For instance, direct dark matter detection experiments probe scatterings of non-relativistic DM particles off nuclei/electrons, and the number of events scales as $N_{\text{events}} \propto \sigma_{\text{scatt}} = g_\chi^2 g^2/m_V^2$. Accelerator experiments that search for scatterings of LDM particles require also its production, and therefore the number of events is $N_{\text{events}} \propto N_{\text{prod}} \cdot \sigma_{\text{scatt}} \propto g^2 \cdot \text{Br}(V \to \text{LDM}) \cdot g_\chi^2 g^2 f(m_V, m_\chi)$. Experiments that search for visible decays of V constrain the combination $N_{\text{prod}} \cdot P_{\text{decay}} \propto g^2 \cdot g^2 \text{Br}(V \to \text{visible})$. Finally, at experiments that search for invisible decays of the mediator bounds, the number of events scales as $g^2 \cdot \text{Br}(V \to \text{LDM})$.

Therefore, we see that in dependence on the scaling $N_{\text{events}} \propto g^\alpha$ there are g^2 experiments and g^4 experiments. In the absence of limitations that are specific to the given search scheme, g^2 experiments are obviously more sensitive to small couplings than g^4 experiments. This is indeed the case for electron fabric experiments such as NA64, Belle/Belle II, and BaBar, which search for events with missing energy/momentum. However, the situation is different for monojet searches at hadron colliders, which suffer from backgrounds and require severe cut on the transverse momentum/missing transverse energy, $p_T \gtrsim 100$ GeV, which is unrealistic for the case of light GeV-scale mediators [126].

LDM with mediators that interact with electrons/photons is strongly constrained by "g^2 experiments": Belle, BaBar, NA64. Such bounds may be diminished if considering models in which mediators do not interact with leptons.

2.3.1 Scattering off nucleons: different signatures

Let us look closer at the LDM scattering off nucleons. This scattering may be mimicked by neutral current (NC) neutrino scattering events, and therefore, such a search is not background-free. Typically, to observe a signal over background, many LDM scattering events are required [127–131]. Under this condition, one can look for an excess of a signal over the numerous neutrino background, and in particular to distinguish events with LDM and neutrinos kinematically by comparing their reconstructed energy spectra. It would be therefore attractive to consider signatures that require less amount of events.

There are two types of LDM scattering off protons: elastic and inelastic, producing an isolated proton or hadronic showers, respectively. For light mediators with masses $m_V \lesssim 1$ GeV, elastic events yield is dominant, while for heavier mediators inelastic scatterings become the main scattering channel. For neutrinos, the dominant channel is inelastic scatterings.

Indeed, both elastic and inelastic differential cross sections depend on the mediator mass m_V as $d\sigma/d\Omega \propto (Q^2 + m_V^2)^{-2}$ due to the propagator, where Q^2 is the momentum transfer. However, the elastic cross section also includes the proton form factor that limits

the possible momentum transfer to $Q^2 \lesssim r_p^{-2} \simeq 1\,\mathrm{GeV}^2$. For large masses m_V, this leads to an additional suppression as compared to the inelastic cross section, to which all $Q^2 \lesssim m_V^2$ contribute without the suppression [131]. As a result, the ratio $\sigma_{\rm el}/\sigma_{\rm inel}$ is a decreasing function of m_V. We illustrate this feature in Fig. 2.20, considering a model of a scalar LDM that interacts with protons via a vector-like mediator. We see that in the case of light mediator $m_V \lesssim 1\,\mathrm{GeV}$, the elastic and inelastic scattering yields may be comparable, and therefore, the elastic signature is more sensitive due to the low background. However, with the increase of m_V, $\sigma_{\rm el}/\sigma_{\rm inel}$ quickly diminishes, and the inelastic signature starts to dominate.

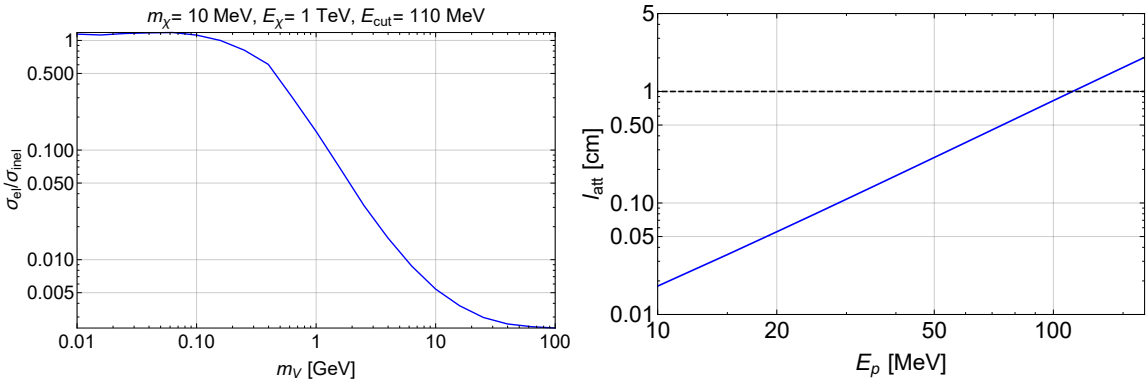

Figure 2.20: *Left panel*: the ratio $\sigma_{\rm el}/\sigma_{\rm inel}$ of elastic and inelastic scattering cross sections in the model with a vector mediator V interacting with protons and a scalar dark sector particle χ of mass $m_\chi = 10\,\mathrm{MeV}$ and energy $E_\chi = 1\,\mathrm{TeV}$. The minimal proton kinetic energy $E_{\rm cut} \gtrsim 110\,\mathrm{MeV}$ is assumed, for which protons may travel 1 cm in tungsten before being absorbed (see text for details). For the description of the elastic and deep inelastic scattering (DIS) used in the estimates, see Appendix 2.C.2. *Right panel:* proton's attenuation length ($l_{\rm att} = \int_0^{E_p} \frac{dE}{dE/dx}$, where dE/dx is the energy loss per unit length) in tungsten as a function of its kinetic energy. The value is calculated using the data from [132].

For masses $m_V \gtrsim m_p$, LDM is more likely to scatter inelastically. In this case, we need to see these events over the numerous neutrino scattering background. A good signature in this case is an increase of the ratio of neutral current and charged current events $N_{\rm NC}/N_{\rm CC}$ for neutrinos. On one hand, it is uniquely predicted within the SM. For the tungsten target, under the approximation of equal differential distributions of ν and $\bar{\nu}$, the ratio $N_{\rm NC}/N_{\rm CC}$ for deep inelastic scattering is equal to [32]

$$P = \frac{1}{2}\left[1 - 2\sin^2\theta_W + \frac{20}{9}\sin^4\theta_W - \lambda(1 - 2\sin^2\theta_W)\sin^2\theta_W\right] \approx 0.33 \qquad (2.3.1)$$

where $\lambda = 0.040$ for the tungsten target. Another advantage of the NC/CC signature is that it is free from the total neutrino flux normalization. This is crucial as it is a subject of theoretical uncertainties for some experiments, for instance, for those at the LHC that are

located in the far-forward direction [133]: currently approved FASER/FASERν [17, 33], and SND@LHC [32].[8]

For LDM particles that scatter of nucleons mostly inelastically, a good search signature at any experiment is an increase of the NC/CC ratio as compared to SM predictions.

2.3.1.1 Model example: leptophobic portal

An example of a model with LDM in which the mediator does not interact with photons and electrons is the leptophobic portal [127, 128, 131, 134, 135]:

$$\mathcal{L}_{\text{leptophob}} = -g_B V^\mu J^B_\mu + g_\chi V^\mu (\partial_\mu \chi^\dagger \chi - \chi^\dagger \partial_\mu \chi), \quad J^B_\mu = \frac{1}{3}\sum_q \bar{q}\gamma_\mu q \tag{2.3.2}$$

Here, g_χ, g_B are coupling constants of the mediator to χ and SM sector, and the sum in J^μ_μ is made over all quark flavors.

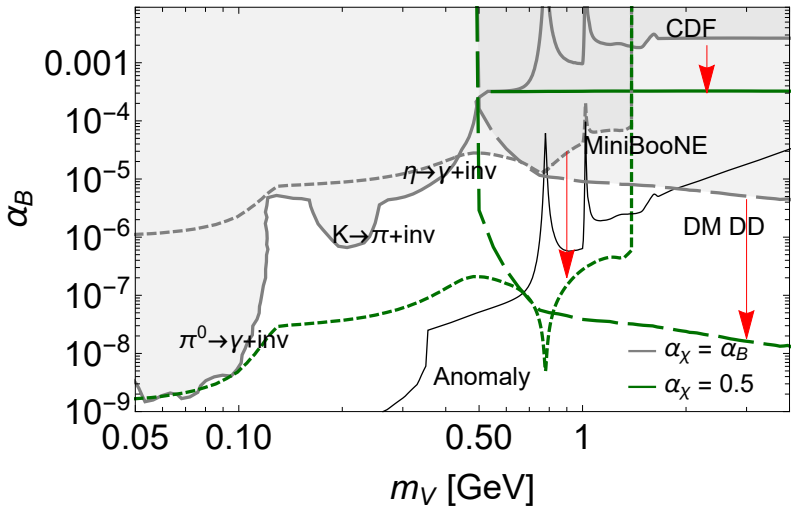

Figure 2.21: Constraints on the leptophobic portal for the case $m_\chi = m_V/3$ and two values of the coupling $\alpha_\chi = g_\chi^2/4\pi$: $\alpha_\chi = \alpha_B$ (in gray) and $\alpha_\chi = 0.5$ (in green). See text for details.

Constraints on the model (2.3.2) are summarized in Fig. 2.21. For $m_V \gtrsim 0.1\,\text{GeV}$, they come from searches for decays $\pi, K, \eta \to V\gamma$ at CB [136], E949 [137], and NA62 [138] experiments (for $m_V \lesssim 0.5\,\text{GeV}$), searches for scattering of χ particles off nucleons at MiniBooNE [139] (for $0.5\,\text{GeV} \lesssim m_V \lesssim 1.5\,\text{GeV}$), a monojet signature analysis at CDF [140] (for $m_V \gtrsim 1.5\,\text{GeV}$), and direct DM searches at CRESST III [34].

The weakness of the CDF monojet signature and the absence of direct constraints from the LHC is caused by the requirement of a large missing transverse momentum

[8] One of goals of these experiments is to study the production of mesons in the far-forward direction.

$p_T \sim 100\,\mathrm{GeV}$ for signal tagging and background suppression. Such large p_T may be provided only by large mass of a decaying particles, which is definitely not the case of light $\mathcal{O}(1\,\mathrm{GeV})$ mediators considered in this section. The bounds from MiniBooNE, being one of the strongest in the region $m_V \lesssim 1\,\mathrm{GeV}$, are much weaker at larger masses due to small center-of-mass energy of the pp collisions, $\sqrt{s} \approx 4\,\mathrm{GeV}$.

Another constraint comes from DM direct detection experiments (DD) [127] that search for scattering of DM particles off nuclei. The sensitivity of these experiments depends on DM particle mass. Indeed, it determines the maximal kinetic energy of DM (which is $T_\chi = m_\chi v_{\text{escape}}^2/2$, where $v_{\text{escape}} = 544\,\mathrm{km/s}$ is the escape velocity), and, therefore, the maximally possible nuclear recoil energy T_N. The DD experiments have finite energy threshold, being $T_N > 30.1\,\mathrm{eV}$ for CRESST-III [34] that is currently the most sensitive experiment. As a result, current constraints from DD are limited by $m_\chi \gtrsim 160\,\mathrm{MeV}$. In addition, the DD bounds may be significantly relaxed even for heavy χ particles if assume their axial-vector interaction with V instead of vector-like one (see [141]) that results in the velocity-suppressed scattering cross section.

Finally, in [142–144], it was argued that the strongest constraint may come from negative results of searches for decays

$$K \to \pi + \text{inv},\ B \to K + \text{inv},\ Z \to \gamma + \text{inv} \tag{2.3.3}$$

at LHCb. In the model of the leptophobic portal (2.3.2), the decays (2.3.3) may result from the anomalous violation of the baryon current conservation, which requires a UV completion in order to cancel the anomaly. Namely, in [142, 143], it was considered a UV completion with some heavy fermions such that the full theory is anomaly-free. At energies much lower than masses of these fermions, the effective theory contains, apart from the Lagrangian (2.3.2), pseudo-Chern-Simons (pCS) interaction operators between V and electroweak bosons W, Z, γ that result from the contribution of massive fermions to the anomalous triangle diagrams. The latter include two summands: a mass-independent, and a mass-dependent. The sum of the first terms over all fermions vanishes due to the anomaly cancellation, while the net mass-dependent part is in general non-zero (for instance, if there is a hierarchy in fermion masses). The corresponding interactions mediate the process $Z \to \gamma + X$, and generate effective flavor changing neutral current couplings bsV, sdV between quarks and the leptophobic mediator (via penguin loop diagrams) that mediate the first two processes in Eq. (2.3.3).

pCS terms generically appear in effective theories with chiral fermions. However, their contribution to the processes (2.3.3) depends on the UV completion of the model (2.3.2). For instance, one could consider a 3+n+1 dimensional model with SM physics localized on a 3+1 dimensional sub-manifold (brane) and a large mass gap for the bulk modes (see e.g. [145, 146]). The higher-dimensional theory is anomaly free by construction without adding extra fermions. The anomaly of the low-dimensional 3+1 effective theory is done by the "anomaly inflow" mechanism, non-local from 3+1 dimensional point of view. In

this case, the anomaly cancellation by massive modes does not contribute to decays.

Due to the model dependence, the status of the anomaly constraint is different from the status of the other bounds discussed above, as the latter require only the effective Lagrangian (2.3.2). Therefore, in Fig. 2.21 we just indicate the parameter space potentially constrained by processes (2.3.3) by showing its lower bound only, while for the other constraints discussed in this subsection the whole parameter space is shown in solid gray.

Choice of parameters. The parameters in the model are LDM particle and mediator masses $m_{\chi,V}$, and the couplings $\alpha_B = g_B^2/4\pi, \alpha_\chi = g_\chi^2/4\pi$.

The of the previous bounds with α_χ is the following. While the scaling of the number of events at MiniBooNE is $N_{\text{events}} \propto \alpha_B \cdot \text{Br}(V \to \chi\bar{\chi}) \cdot \alpha_B \cdot \alpha_\chi$, the number of events at the other experiments scales as $N_{\text{events}} \propto \alpha_B \cdot \text{Br}(V \to \chi\bar{\chi})$ for the collider experiments and $\alpha_B \cdot \alpha_\chi$ for DD experiments (remind the discussion in the beginning of Sec. 2.3).[9]

Further, we consider two values of α_χ. The first one is $\alpha_\chi = \alpha_B$, which is typically considered in the literature, and for which $N_{\text{events}} \propto \alpha_B^3 \cdot \text{Br}(V \to \chi\bar{\chi})$ at the accelerator direct detection experiments. The second one is $\alpha_\chi = 0.5$, for which $N_{\text{events}} \propto \alpha_B^2$.

Let us now comment on the choice of m_χ. As we have discussed previously, masses $m_\chi > 160\,\text{MeV}$ are significantly constrained by the DM direct detection experiments. Therefore, we consider two different choices: $m_\chi = m_V/3$, which is commonly used in literature and for which the DD constraint is important above $m_V = 480\,\text{MeV}$, and $m_\chi = 20\,\text{MeV}$, for which there is no bound from DD at all.

2.3.2 SND@LHC

2.3.2.1 Description of experiment

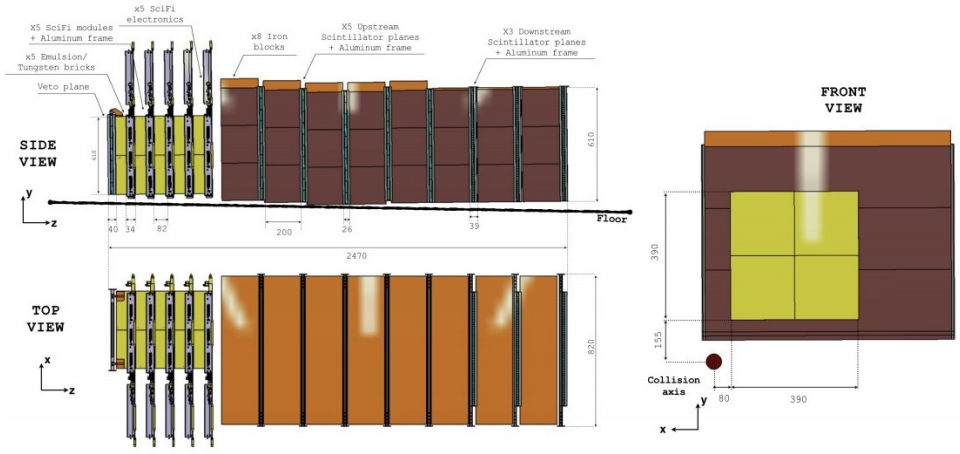

Figure 2.22: Overview of the SND@LHC detector facility: the side view (on the left) and the front view (on the right). The figure is taken from [32].

[9] For the calculation of the branching ratio $\text{Br}(V \to \chi\bar{\chi})$, see Appendix 2.C.

SND@LHC facility is planned to be installed in the TI18 tunnel at the distance of 480 m from the ATLAS interaction point along the beam collision axis. The SND@LHC detector consists of the target region followed by the muon system, see Fig. 2.22. The pseudorapidity range covered by the target will be $7.2 < \eta < 8.6$, in which ν_e, ν_τ are produced in decays of heavy mesons, with an additional component of muon neutrinos originated from decays of pions and kaons. The actual angular position of the target is $(\theta_x, \theta_y) \in [0.17, 0.98] \times [0.32, 1.14]\,\mathrm{mrad}^2$.

The target has brick structure: bricks of emulsion cloud chambers (ECC) followed by Scintillating Fibre (SciFi) plates. Each of five emulsion bricks consists of 60 emulsion films interleaved with 59 tungsten plates of 1 mm thickness, which serve as target. The total scattering length of the emulsion bricks is $29.5\,\mathrm{cm}$, which corresponds to 84 radiation lengths (X_0), and the total target length of about $40\,\mathrm{cm}$. The ECC provide micrometric accuracy that allows one to measure accurately tracks of charged particles, and reconstruct vertices of neutrino interactions (for events without muons) and any other event that deposit their energy within one emulsion brick.

SciFi predicts the neutrino interaction vertex location, connects the emulsion track with the muon track identified by the muon detector, and provides timing information for the events (with timing resolution of the order $100\,\mathrm{ps}$). In this way, it serves for disentangling the piled up events occurring in one emulsion layer. In addition, the whole facility works as a hadronic calorimeter with 9-11 interaction lengths.

An important feature of SND@LHC is high neutrino type identification efficiency. The target construction allows track detection of charged particles produced in primary interactions and subsequent decays. Muons are identified as the most penetrating charged particles, while τ-leptons – via a displaced vertex with an electron or a muon track.

There are two phases of the event reconstruction at SND@LHC [32]. The first phase uses electronic detectors: events are reconstructed based on veto, the target tracker and the muon system. The second phase adopts the emulsion target, and the event reconstruction will be available six months after the exposure. It identifies EM showers, complements the target tracker for EM energy measurements, and allows for the neutrino vertex reconstruction. The matching between these phases is required for events containing muons; it is the subject of ongoing studies.

Although the main goal of SND@LHC is to probe high-energy neutrino scatterings, it may also search for scatterings for LDM and probably even for decays of mediators.

Below, we illustrate the potential of SND@LHC to probe FIPs via decays and scatterings by estimating the sensitivity to several models. We consider two experimental setups of the detector: one that will operate during Run 3, and a possible upgrade that will work during Run 4 (see [32]). Their parameters are summarized in Table 2.3.

Setup	$\mathcal{L}$, fb^{-1}	$l_{\rm det}^{\rm scatt}$, cm	$l_{\rm det}^{\rm decay}$, cm
Setup 1	150	30	50
Setup 2	3000	75	125

Table 2.3: Experimental setups of the SND@LHC detector used in this work. The parameters are the integrated luminosity $\mathcal{L}$, the detector's length available for scatterings $l_{\rm det}^{\rm scatt}$, the detector's length available for decays $l_{\rm det}^{\rm decay}$. See text for details.

2.3.2.2 Search for scatterings of LDM

Let us discuss signal efficiency and background at SND@LHC for the *elastic signature*.

> Even a few of LDM elastic scattering events would lead to observable deviation from SM predictions at SND@LHC.

According to [32], the selection criterion for the elastic scattering off protons is a single isolated track with the momentum $p > 170\,\mathrm{MeV}$ observed in the emulsion. Studies of MC simulation containing produced particles prior to their interaction with the detector have shown that once this selection is applied to events with neutrinos, the only surviving background comes from neutrino NC resonant and deep inelastic scatterings, where only one charged track is visible, with the total number of events being 1.7. To overcome this background with 2σ CL, we require 5 elastic events.[10]

At the same time, low-momentum protons with $p \simeq 170\,\mathrm{MeV}$ that satisfy the selection criterion considered in [32] have small attenuation length[11] in tungsten, $l_{\rm att} \lesssim 1\,\mathrm{mm}$, and get absorbed in the single tungsten plate before reaching the emulsion [147]. Therefore, this requirement is not appropriate for estimate of the number of elastic χ scatterings that can be detected. Instead, for LDM signature, we require proton kinetic energy $E_p > 110\,\mathrm{MeV}$, for which protons have attenuation length $l_{\rm att} = 1\,\mathrm{cm}$, and therefore may pass through ten emulsion layers, see Fig. 2.20. We note that this criterion is conservative and may be further relaxed.

Since the requirement on the proton energy is more tight than the one assumed in the simulation in [32], the background would be lower and can go down to zero. However, precise background estimates require additional studies. Therefore, we conservatively assume the same number of background events as for the looser requirement of $p > 170\,\mathrm{MeV}$ as in [32].

Still, even with the stronger cut, such protons may not reach SciFi plates, which may lead to piled up events and potentially decrease the efficiency of the reconstruction of the signal. Namely, there may be a coincidence between the neutrino and χ scattering events,

[10] We estimate it using the relation $\sum_{n_{\rm ev}=0}^{\infty} P(n_{\rm ev}|b+s)P(n \geq n_{\rm ev}|b) < 4.5\%$, where $b = 1.7$ is the background, s is the signal, and P is the Poisson distribution.

[11] Contrary to high-energy protons that produce hadronic cascades, protons with low energies lose this energy electromagnetically and travel around $\mathcal{O}(1\,\mathrm{cm})$ in tungsten before being absorbed [52].

accumulated during six months of the SND emulsion phase operation period. However, in practice this feature does not affect the efficiency. The expected amount of neutrino events at SND@LHC during Run 3 is $\simeq 2 \cdot 10^3$ [32]. Since the DIS event may be reconstructed by the single emulsion layer, for estimating of the pile up effect we are interested in the number of neutrino events per layer, instead of their total amount. During six months of the operation period and given that the SND target consists of 60 emulsion layers, only 6 neutrino events will occur per each layer. Taking into account the micrometric accuracy of the emulsion, this amount is vanishingly small to affect the signal.

Let us comment on effects that have not been included in the simulation discussed in [32]. The first effect is a possible background from neutrino DIS events, in which soft particles get absorbed in tungsten layer before reaching the emulsion. As a result, the DIS event may mimic an elastic scattering event. However, this effect can be neglected, as high-energy neutrinos typically deposit large amount of energy in their scattering leading to many tracks in the event. Indeed, assuming the operating period corresponding to the LHC Run 3, the MC simulations in [32] have shown no events of neutrino DIS with only one track having $E > 110\,\mathrm{MeV}$ and all other tracks with energies $E \ll 100\,\mathrm{MeV}$ (such that they may be absorbed in tungsten before reaching the emulsion layer) that would be recognized as an elastic event. The second effect is a proton-to-neutron conversion, which may reduce the signal from the elastic scattering. However, the nuclear interaction length in tungsten, which is a characteristic scale of the conversion, is $\mathcal{O}(5\,\mathrm{cm})$ corresponding to about 50 emulsion layers in the target. Therefore, the proton would produce a visible track in large fraction of events, and this process will not affect the elastic event reconstruction. Finally, the third effect is possible background from radioactive isotopes that may be hypothetically present in the target. However, the decay products are typically low-energy, as energy release for most isotopes does not exceed $10\,\mathrm{MeV}$, and therefore, they get absorbed in the single tungsten layer without being detected.

For masses $m_V \gtrsim m_p$, LDM is more likely to scatter inelastically, and we consider the *NC/CC signature*.

For the NC/CC signature, the required number of events at SND@LHC is $\mathcal{O}(100)$ at 2σ confidence level.

Indeed, SND@LHC claims to measure the NC/CC ratio with the precision of 10%. Assuming $N_{\mathrm{CC}}^{\mathrm{SND@LHC}} = 1395$ and $N_{\mathrm{NC}} = 450$ as predicted by simulations for the SND@LHC setup [32], we require the yield of LDM inelastic scattering events to be $2\sqrt{450 + 45.0^2} \approx 100$ in order to reach the 2σ confidence level.

2.3.2.3 Search for decays of mediators

Although SND@LHC is constructed to probe neutrino scatterings, it may also be capable of searching for decays of FIPs, for instance scattering mediators. It is attractive to probe the parameter space simultaneously by scatterings of LDM and decays of mediators.

However, for the given coupling g, the decay length of the mediator is typically much shorter than the scattering length of LDM particles. Because of this, it is typically not possible to probe decays of mediators and scatterings of LDM within the same domain of parameter space.

Indeed, consider scatterings and decays using as an example vector (dark photons) and scalar portals. The scattering probability is

$$P_{\text{scat}} = \sigma_{\text{scat}} n_{\text{atom}} L_{\text{det}}, \qquad n_{\text{atom}} \sim (1\,\text{keV})^3 \tag{2.3.4}$$

with the scattering cross section

$$\sigma_{\text{scat}} \sim \frac{\alpha_{S\chi\chi} y_N^2 \theta^2}{m_N E_\chi}\ (\text{scalar}), \qquad \sigma_{\text{scat}} \sim \frac{\alpha_D \epsilon^2}{m_V^2}\ (\text{vector}) \tag{2.3.5}$$

In its turn, the decay probability is

$$P_{\text{dec}} = \frac{\Gamma L_{\text{det}}}{\gamma}, \qquad \Gamma \sim \theta^2 \frac{m_S^3}{v^2}\ (\text{scalar}), \qquad \Gamma \sim \epsilon^2 m_V\ (\text{vector}) \tag{2.3.6}$$

Comparing these two probabilities, one gets

$$\frac{P_{\text{scat}}}{P_{\text{dec}}} \sim \gamma \alpha_{S\chi\chi} y_N^2 \left(\frac{v}{m_S}\right)^2 \frac{n_{\text{atom}}}{m_S m_N E_\chi}\ (\text{scalar}), \qquad \frac{P_{\text{scat}}}{P_{\text{dec}}} \sim \gamma \alpha_D \frac{n_{\text{atom}}}{m_V^3}\ (\text{vector}) \tag{2.3.7}$$

As a result, for large couplings, that are required to see scatterings, the decay length is microscopic, and mediators decay before reaching the detector. It may be still possible though to probe large couplings via scatterings of LDM and smaller couplings via decays of the mediator.

There are potentially background-free signatures of mediators decays at SND@LHC. These are decays into a di-lepton pair, into a lepton and a meson, or into two mesons.

Indeed, a clear background-free signature may be decays of a FIP into a di-lepton pair, $V \to ll'/ll'\nu$, as scatterings of neutrinos produce at most one lepton.[12] For the decays of FIPs into a lepton and a meson, or into a pair of mesons there is a background that comes from the neutrino deep inelastic CC- and NC-scatterings correspondingly. However, decay products typically carry large energies $E \gtrsim 100\,\text{GeV}$ and, therefore, can be distinguished from (inelastic) neutrino scatterings with such large energy transfers as the latter typically

[12]The di-muon events may be produced by the scattering of photons in the detector. However, the photons occur in scattering of neutrinos, and apart from the di-muon pair there would be a lot of other tracks.

produce a lot of hadrons. Therefore, we believe that the mentioned background may be rejected. This question requires an additional study.

To use these signatures, it is necessary to disentangle tracks from decays of FIPs. At the SND@LHC detector, this is possible if the transverse distance between the tracks exceeds the spatial resolution, which is of the order of $1\,\mu\mathrm{m}$ for the emulsion films. The transverse distance between two tracks is determined by the flight angle that can be estimated as $\Delta\theta \simeq \frac{m_{\text{FIP}}}{E_{\text{FIP}}}$, and the distance l charged particles travel inside the target. For electrons, l is the radiation length, which in tungsten is equal to $3.5\,\mathrm{mm}$. Muons pass through the whole target without deflection, and therefore, we may conservatively restrict l to the thickness of a single SND@LHC emulsion brick $7.8\,\mathrm{cm}$. For FIPs flying in the far-forward direction, the typical energy is $E_{\text{FIP}} \simeq 1\,\mathrm{TeV}$. Thus, the corresponding masses are

$$m_{\text{FIP}} \gtrsim \min\left[E_{\text{FIP}}\,\frac{1\,\mu\mathrm{m}}{l}, 2m_{e\text{ or }\mu}\right] \simeq \begin{cases} 290\,\mathrm{MeV}, & \text{FIP} \to e\bar{e} \\ 210\,\mathrm{MeV}, & \text{FIP} \to \mu\bar{\mu} \end{cases} \tag{2.3.8}$$

If the disentanglement is not possible, instead of tracks we observe a mono-cascade. A similar signature may come from FIPs decaying into neutral pions, such as from HNLs that mix with tau flavor that decay into π^0 and a neutrino. This type of events may still be distinguished from neutrino scatterings, as the latter typically contain many tracks, and hence may be a new physics signature.

Background evaluation and event reconstruction for both charged pair and monocascade signatures are challenging tasks and require dedicated studies. Further, we will show the fixed signal events contours, assuming that all events are detected.

2.3.3 Sensitivity of SND@LHC

2.3.3.1 Leptophobic portal

Let us now estimate the sensitivity of SND@LHC to LDM scattering in the model (2.3.2). The number of scattering events may be estimated using the formula

$$N_{\text{events}} = 2\cdot N_{\chi}^{\text{SND@LHC}} \times n_{\text{detector}} \times \begin{cases} Z\cdot\sigma_{\text{scatt}}^{\text{el}}(\langle E_\chi\rangle)\cdot l_{\text{det}}^{\text{scatt}}, & \text{elastic signature} \\ A\cdot\sigma_{\text{scatt}}^{\text{inel}}(\langle E_\chi\rangle)\cdot l_{\text{det}}^{\text{scatt}}, & \text{inelastic signature} \end{cases} \tag{2.3.9}$$

Here, $N_{\chi}^{\text{SND@LHC}}$ is the number of χ particles produced in the direction of the SND@LHC detector volume (a factor of 2 stays for $\bar{\chi}$), n_{detector} is the detector's atomic number density (the tungsten material is considered), Z, A are atomic and mass numbers of the target material, and $\sigma_{\text{scatt}}^{\text{el/inel}}$ is the elastic or inelastic scattering cross section of χ particles. For simplicity, in cross section calculation we assume that all χ particles have the same energy equal to their average energy $\langle E_\chi\rangle$.

We adopt the description of the elastic scattering process from [134]. For the estimate of the cross-section for inelastic scattering, we use the calculation based on the parton model from [148], for which parton distribution functions are given by CT10nlo PDF sets from LHAPDF package [149] (see also Appendix 2.C.2).

Let us now consider the production of χ particles. The $\chi\bar{\chi}$ pairs originate from decays of V. Similarly to the dark photon case, the mediator may be produced:

1. in decays of unflavored mesons π, η,

$$\pi \to V + \gamma, \quad \eta \to V + \gamma, \tag{2.3.10}$$

2. by proton bremsstrahlung,

$$p + p \to V + X, \tag{2.3.11}$$

3. in Drell-Yan process,

$$q + \bar{q} \to V + X, \tag{2.3.12}$$

see Fig. 2.23. For the description of these channels, we mainly follow [144, 150, 151].

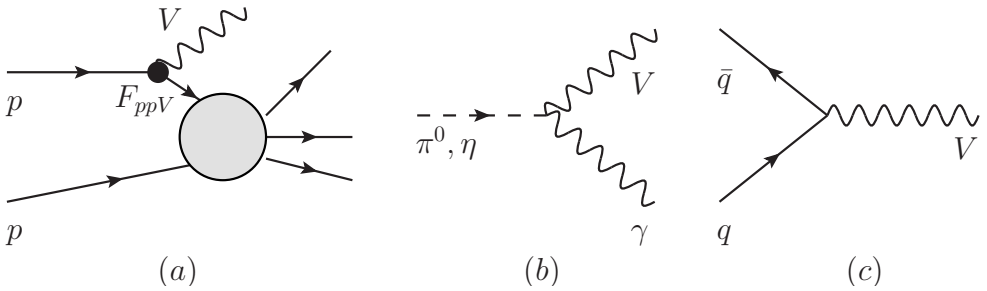

Figure 2.23: Diagrams of the production of the leptophobic mediator V: by proton bremsstrahlung (a), in decays of light unflavored mesons (b), and in Drell-Yan process (c).

For the production from mesons, we use the polar angle and energy distributions of π, η mesons generated by EPOS-LHC [152] as a part of the CRMC package [153]. The resulting spectra of V and χ particles are obtained semi-analytically using an approach presented in [120].

For obtaining the angle-energy distribution of the leptophobic mediator produced by the proton bremsstrahlung, we consider the kinematic range $p_T < 1\,\mathrm{GeV}$ and $0.1 < z < 0.9$. The corresponding production probability is affected by the mixing of V with isoscalar ω and ϕ mesons. To describe this effect, we follow the procedure described in [154] (see Appendix 2.C for details). The distribution of subsequent χ particles produced by the bremsstrahlung is obtained in a similar way as for the case of the production from mesons.

For the production in the Drell-Yan process, we use our implementation of the model (2.3.2) in MadGraph5 [113] with FeynRules [117, 118]. We then obtain the geo-

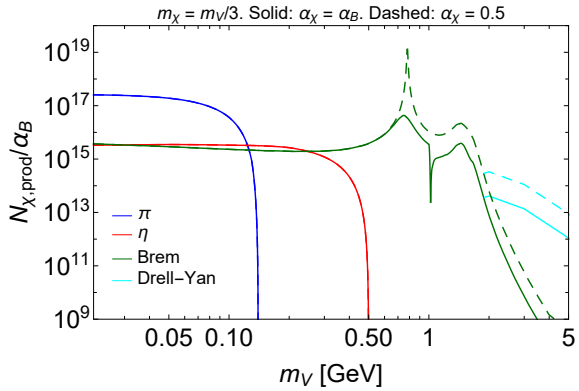

Figure 2.24: The number of χ particles produced in the direction of the SND@LHC experiment, assuming the integrated luminosity $\mathcal{L} = 150\,\mathrm{fb}^{-1}$. $m_\chi = m_V/3$ is assumed. Wiggles around V masses of $782\,\mathrm{MeV}, 1020\,\mathrm{MeV}$ and $\simeq 1.7\,\mathrm{GeV}$ are caused by the mixing of the mediator with isoscalar vector mesons ω, ϕ, and their excitations, which leads to the resonant enhancement of 1) the ppV form-factor for the production by the proton bremsstrahlung, and 2) the decay width of the leptophobic mediator V into hadrons (and hence to a suppression of $\mathrm{Br}(V \to \chi\bar{\chi})$). See text and Appendix 2.C for details.

metric acceptance and energy distribution of χ particles traveling into the direction of the SND@LHC detector by simulating the leading-order process $p + p \to V,\ V \to \chi\bar{\chi}$.

We find that the main production channel for masses $m_V \lesssim m_\eta$ is decays of mesons, for masses $m_\eta \lesssim m_V \lesssim 3\,\mathrm{GeV}$ is the proton bremsstrahlung, and, finally, for $m_V \gtrsim 3\,\mathrm{GeV}$ it is the Drell-Yan process, see Fig. 2.24.

Most of the produced χ particles have γ factors $\sim 10^3$, independently of the production channel. This means that the time-of-flight measurement is not efficient in separating signal χ particles and neutrinos.

Sensitivity. Let us now discuss the sensitivity. The parameters in the model are LDM particle and mediator masses $m_{\chi,V}$, and the couplings $\alpha_B = g_B^2/4\pi, \alpha_\chi = g_\chi^2/4\pi$.

The choice of α_χ affects the parameter space probed by SND@LHC in the following way. The number of scattering events at SND@LHC scales as

$$N_{\mathrm{events}} \propto \alpha_B \cdot \mathrm{Br}(V \to \chi\bar{\chi}) \times \alpha_B \cdot \alpha_\chi \tag{2.3.13}$$

Here, a factor $\alpha_B \cdot \mathrm{Br}(V \to \chi\bar{\chi})$ comes from the production, while a factor $\alpha_B \cdot \alpha_\chi$ – from the subsequent scattering of χ particles. The scaling of the previous bounds is somewhat different. While the scaling of events at MiniBooNE is similar, the number of events at the other experiments scales as $N_{\mathrm{events}} \propto \alpha_B \cdot \mathrm{Br}(V \to \chi\bar{\chi})$ for the collider experiments and $\alpha_B \cdot \alpha_\chi$ for DD experiments. Therefore, the dependence on α_B and α_χ is weaker.[13] Therefore, marginalizing over α_χ, the optimal choice would be $\alpha_\chi \simeq 1$, for

[13]For the calculation of the branching ratio $\mathrm{Br}(V \to \chi\bar{\chi})$, see Appendix 2.C.

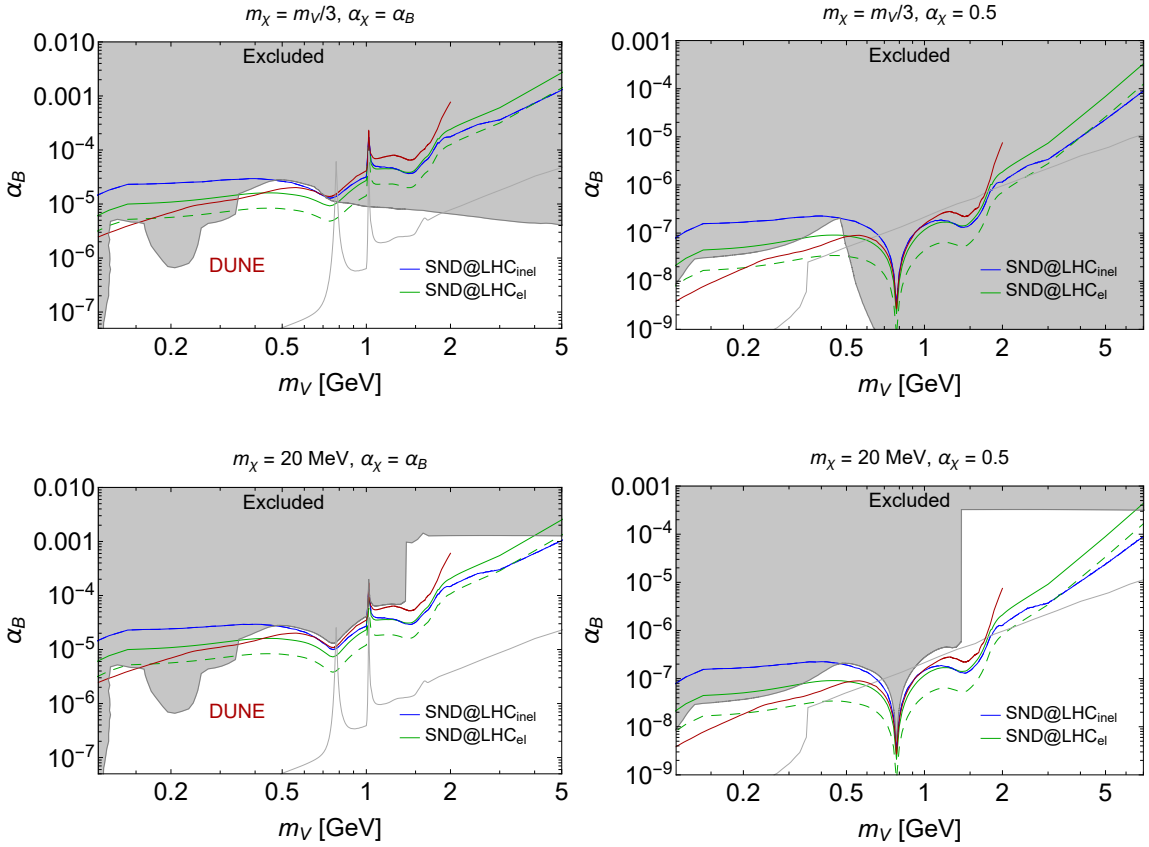

Figure 2.25: Sensitivity of the SND@LHC experiment to the leptophobic portal (2.3.2) (2σ CL). The sensitivity is shown under an assumption $m_\chi = m_V/3$ (top panel) and $m_\chi = 20\,\mathrm{MeV}$ (bottom panel), and for two different choices of the coupling of mediator to χ particles: $\alpha_\chi = \alpha_B$ (left figures), and $\alpha_\chi = 0.5$ (right figures). The considered signatures are the elastic scattering off protons (the green line) and the deep-inelastic scattering (the blue line, corresponding to 100 signal events during Run 3), see text for details. For the elastic signature, the solid line corresponds to the sensitivity during Run 3 (corresponding to 5 signal events), while the dashed line denotes the sensitivity of the upgraded setup that may operate during Run 4 (see text for details). We assume that the level of background to the elastic signature during Run 3 is 1.7 events, as reported in [32] for much weaker cut on the proton's momentum $p > 170\,\mathrm{MeV}$ that the cut used in our estimate, $p \gtrsim 500\,\mathrm{MeV}$. Therefore, the sensitivity is conservative. By the red line, we show the 100 event contour for the DUNE experiment from Ref. [130]. We rescale the previous bounds according to our description of the proton form-factor used in bremsstrahlung and $\mathrm{Br}(V \to \chi\chi)$. The thin gray line corresponds to model-dependent constraints from invisible decays (2.3.3) as derived in [144] (see text for details).

which SND@LHC would probe larger range of mediator masses.

The sensitivity of the SND@LHC experiment to the leptophobic portal for two different setups from Table 2.3 is shown in Fig. 2.25. Following the discussion in Sec. 2.3.2.2, we require $N_{\text{events}} > 5$ for the elastic signature and $N_{\text{events}} > 100$ for the inelastic signature

during Run 3.

The parameter space that may be probed by SND varies in dependence on the values of parameters α_χ, m_χ. Namely, for the choice $m_\chi = m_V/3$, SND@LHC only may probe masses $350\,\text{MeV} < m_V < 700\,\text{MeV}$. For the choice $m_\chi = 20\,\text{MeV}$, it is possible in addition to probe masses $700\,\text{MeV} < m_V \lesssim 7\,\text{GeV}$. Moreover, for the choice $\alpha_\chi = 0.5$, the probed range of the coupling α_B even competes with the model-dependent bound from the signature $B \to K +$ inv at the lower bound.

Unlike the case of the direct detection experiments, the sensitivity of SND@LHC depends only weakly on the choice of m_χ, as the production probability and the scattering cross section of χ particles is determined mainly by m_V. In this way, SND@LHC and direct DM detection experiments may probe complementary mass ranges of χ.

In the figure, we also show the sensitivity of DUNE experiment from [130]. The background estimate has not been made for this experiment. Therefore, we show the contour corresponding to 100 events.

Finally, let us discuss the improvement of the sensitivity of SND@LHC for the upgraded setup. For the curve describing elastic scattering signature, the scaling of the lower bound of the sensitivity with the integrated luminosity $\mathcal{L}$ and detector length $l_{\text{det}}^{\text{scatt}}$ is

$$\alpha_B^{\text{el}} \propto \left(N_{\chi,\text{prod}}^{\text{SND@LHC}} \cdot l_{\text{det}}^{\text{scatt}} / \sqrt{N_{\text{bg}}} \right)^{-1/n} \propto (\mathcal{L} \cdot l_{\text{det}}^{\text{scatt}})^{-1/n}, \tag{2.3.14}$$

where the scaling of the number of neutrino background events is $N_{\text{bg}} \propto \mathcal{L} \cdot l_{\text{det}}^{\text{scatt}}$, and $n = 2$ or 3, depending on the choice for α_χ. The improvement of the sensitivity for the upgraded setup reaches a factor of 2 to 3. We note, however, that due to tighter requirement on the proton energy used in our estimate, the elastic signature may be background-free, in which case the improvement increases by up to a factor 10. For the inelastic signature, the scaling depends on the improvement of the uncertainty in the NC/CC ratio measurement during the time frame of the upgraded setup. In the optimistic scenario, the uncertainty will be significantly smaller, and the lower bound will become better by the same factor as for the elastic signature.

2.3.3.2 Decays

To illustrate the potential of SND@LHC to probe decays, we estimate the sensitivity to scalar, neutrino and vector portals, which introduce correspondingly a light Higgs-like scalar, a heavy neutral lepton (HNL) and a dark photon (see, e.g., [67] for the description of the models). Decays with pairs of charged particles in the final state – muons, electrons and pions – are the main decay channels for all the portal particles, except for GeV scale HNLs N that mix with ν_τ, for which the main decay channel is a decay $N \to \pi^0 \nu$.

In order to obtain the sensitivity of SND@LHC to various decaying FIPs, we use the following estimate:

$$N_{\text{events}} = \sum_{\text{i}} N^i_{\text{prod}} \cdot \epsilon^i_{\text{geom}} \cdot P^i_{\text{decay}} \cdot \text{Br}_{\text{vis}} \tag{2.3.15}$$

Here, N^i_{prod} is the total number of FIPs of species X produced via channel i, ϵ^i_{geom} is the geometric acceptance for particle X decay products, and P^i_{decay} is the decay probability averaged over energies E_X of particles X,

$$P^i_{\text{decay}} = \int (e^{-l_{\text{min}}/c\tau_X\gamma_X} - e^{-l_{\text{max}}/c\tau_X\gamma_X}) f^i_{E_X} \mathrm{d}E_X, \tag{2.3.16}$$

with f_{E_X} being the energy E_X distribution of FIPs that fly in the decay volume, and τ_X and γ_X their lifetime and Lorentz boost factor, respectively. Finally, Br_{vis} is the branching ratio of visible decays of particle X. Details of estimates are summarized in Appendix 2.B. The sensitivities are shown in Fig. 2.26, where we show the estimate for the Run 3 setup, as well as for the possible upgrade that may operate during Run 4. For the upgraded setup, the number of events at the lower bound is higher by a factor of $l^{\text{dec}}_{\text{det,upgr}}/l^{\text{dec}}_{\text{det}} \cdot \mathcal{L}_{\text{Run 4}}/\mathcal{L}_{\text{Run 3}} = 50$.

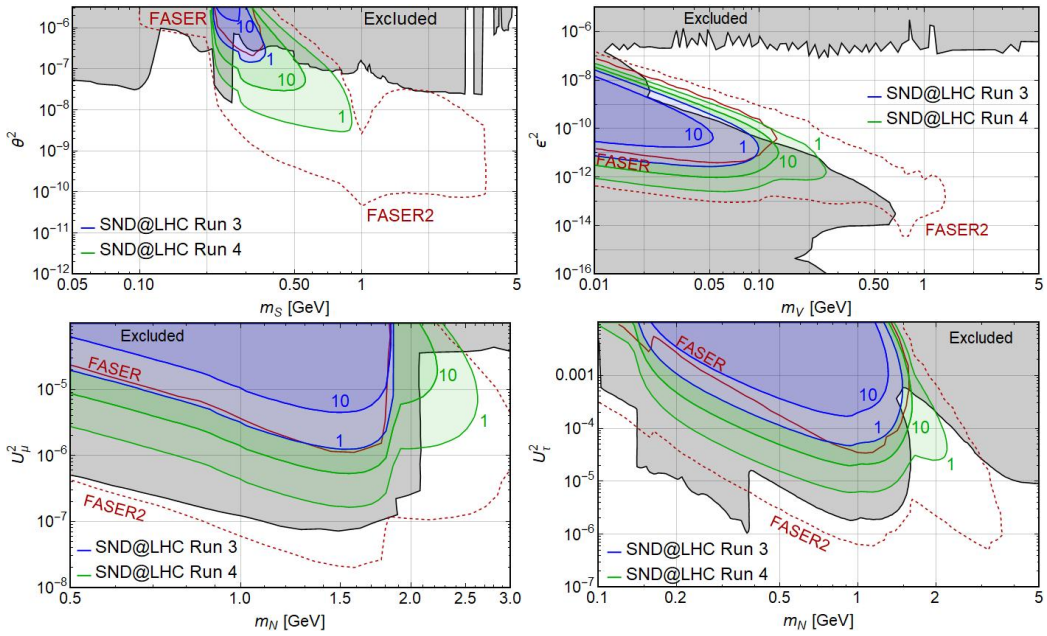

Figure 2.26: Sensitivity of SND@LHC to (top left) dark scalars, (top right) dark photons, and HNLs that mix with (bottom left) ν_μ and (bottom right) ν_τ. Blue (green) contours correspond to 1 and 10 events in the (upgraded) SND@LHC target. Sensitivities of previous experiments and of the FASER/FASER2 experiment are reproduced from [58, 67].

We conclude that for the Run 3 setup, SND@LHC may probe only a tiny parameter space for dark scalars, dark photons and HNLs that mix with τ flavor. For the upgraded setup, it may be possible to probe HNLs that mix exclusively with ν_μ in the mass range $\lesssim 2.5\,\text{GeV}$, and in $\lesssim 2.0\,\text{GeV}$ for pure mixing with ν_τ. SND@LHC may also probe dark

photons at the upper bound of the sensitivity with masses $m_V \lesssim 0.1\,\mathrm{GeV}$, and dark scalars with masses $m_S \lesssim 0.8\,\mathrm{GeV}$.

2.3.4 Comparison with FASER

There is a similarity between the facilities of SND@LHC and FASER/FASERν experiments. They are both placed in a large η region and at the same distance $l_{\text{min}} = 480$ m from the ATLAS interaction point, but in the opposite tunnels. Parameters of the experiments are summarized in Table 2.4. Below, we make a qualitative comparison of the sensitivities of the SND@LHC and FASER experiments, and then comment on the changes due to upgrades.

Detector	l_{min}, m	l_{det}, m	θ_{min}, mrad	θ_{max}, mrad	$\Omega \cdot 10^7$, sr	$\mathcal{L}, \text{fb}^{-1}$
SND@LHC	480	0.5	0.3	1.5	6.9	150
FASER		1.5	0.	0.2	1.4	
FASERν		1.	0.	0.4	2.7	
SND@LHC upgr.		1.25	0.3	1.5	6.9	3000
FASER2		5	0.	2.1	138	

Table 2.4: Parameters of SND@LHC and FASER experiments: the distance to the decay volume, the length of the decay volume, the polar coverage, covered solid angle, total integrated luminosity.

Let us summarize the main differences between SND@LHC and FASER/FASERν detectors in the reconstruction of signal. For scattering, SND@LHC competes with the FASERν detector. FASERν consists of emulsion films interleaved with tungsten plates, only providing the information of spatial position of different tracks with 30% energy reconstruction accuracy for neutrino events (see also [155]). For muons, the situation is much better, as they, being produced in FASERν, may penetrate it and enter FASER, which allows timing and momentum measurements. This option is unavailable, however, for other particles (hadrons, electrons), as they are effectively absorbed in the detector. On the contrary, SND@LHC provides timing measurements by the use of the SciFi technology and the energy reconstruction accuracy of 22% for electrons. For both experiments, timing is needed for rejecting the background induced by high-energy muons and secondary particles.[14]

In the case of decays, SND@LHC competes with FASER, and their detectors provide comparable FIP parameters reconstruction accuracy, thanks to good spatial resolution of the emulsion. Assuming that SND@LHC is a background free experiment when searching for decays, the only relevant quantity for comparing the experiments is the number of correctly identified FIP decay events.

[14] In this work, we compare the signal of new physics to the number of neutrino interactions, which was already obtained under assumption of possible background. Therefore, these key features of the detectors' concept are omitted in our analysis.

2.3.4.1 Lower and upper bound of the sensitivity

Let us now consider the differences in the number of events at these experiments. Two factors are important. First, SND@LHC is slightly off-axis, whereas FASER(ν) is placed directly on-axis. Second, SND@LHC covers $\simeq 5$ (1.25) times larger solid angle than FASER(ν).

The different placements of SND@LHC and FASER/FASERν cause two effects that directly affect the lower and upper bound of the sensitivity (we follow [9] here): *(i)* off-axis placement of SND@LHC causes smaller γ factor and thus worse potential to probe the parameter space of short-lived FIPs; *(ii)* large angular coverage leads to larger fraction of particles from heavy mesons flying to the detector.

First, particles X flying off-axis have smaller energies than those flying on-axis. This is important for probing FIPs that have small decay lengths $l_{\text{decay}} \lesssim l_{\text{min}}$. Indeed, in this regime, the decay probability is $P_{\text{decay}} \approx \exp[-l_{\text{min}}/c\tau_X\gamma_X]$. The sensitivity to such large couplings g determines the upper bound, which is very sensitive to the mean energy of X:

$$\frac{g^2_{\text{upper,SND@LHC}}}{g^2_{\text{upper,FASER}}} \sim \frac{\gamma_X^{\text{SND@LHC}}}{\gamma_X^{\text{FASER}}} \tag{2.3.17}$$

The upper bound is important for particles that may be probed by the FASER and SND@LHC experiments only in the regime of small decay lengths, including dark photons and axion-like particles (see Fig. 2.26). The ratio of the mean γ-factors of dark photons A', flying in the detector, is $\gamma_{A'}^{\text{SND@LHC}}/\gamma_{A'}^{\text{FASER}} \approx 1/3$. The resulting estimate (2.3.17) agrees with the sensitivities in Fig. 2.26.

Second, the off-axis placement may affect the geometric acceptance. Light portal particles X are often produced in decays of mesons. The angular distribution of particles X is similar to the distribution of parent mesons at angular scales larger than $\Delta\theta \simeq 2p_{X,\text{rest}}/\langle E_{\text{meson}}\rangle$, where $p_{X,\text{rest}}$ is the momentum of the daughter particle at rest frame of the decaying meson, being $\simeq m_{\text{meson}}$ if masses of all decays products are $\ll m_{\text{meson}}$. If $\Delta\theta > \theta_{\text{SND@LHC}} \simeq \mathcal{O}(1\,\text{mrad})$, the ratio of geometric acceptances ϵ_{geom} for the SND@LHC and FASER experiments scales with their solid angle coverage. Using characteristic energies $\langle E_{\text{meson}}\rangle \simeq 1\,\text{TeV}$ for mesons produced in the far-forward region, we find that this scaling is indeed the case of light particles produced in decays of D, B-mesons.

However, if the daughter particle is heavy $m_X \simeq m_{\text{meson}}$, or if the decaying meson is light (such as π, η, K), the geometric acceptance depends on the shape of the meson distribution. Experimental measurements of the meson production cross section in the region $|\eta| < 5$ [156–159] provide the following scaling:

$$\frac{\text{d}\sigma}{\text{d}p_{\text{T}}} \sim \frac{p_{\text{T}}}{(p_{\text{T}}^2 + \Lambda^2_{\text{meson}})^2}, \tag{2.3.18}$$

independently of the pseudorapidity. The values of Λ_{meson} are of order of $\Lambda_{\text{QCD}} \approx 250\,\text{MeV}$ for light mesons π, η, K, and $m_{D/B}$ for D/B-mesons. Numeric approaches (see, for instance, [43, 152, 160, 161]) predict the same behavior of $\mathrm{d}\sigma/\mathrm{d}p_{\text{T}}$ almost independently of pseudorapidity, including the far-forward region.[15] This means that the meson distribution $\mathrm{d}f/\mathrm{d}\Omega$ is flat for angles $\theta \lesssim \theta_{\text{flat}}$, where

$$\theta_{\text{flat}} \sim \frac{\langle p_{\text{T}} \rangle}{\langle E_{\text{meson}} \rangle} \sim \frac{\Lambda_{\text{meson}}}{1\,\text{GeV}}\text{mrad} \simeq \begin{cases} \mathcal{O}(1\,\text{mrad}), & B, D \\ \mathcal{O}(0.1\,\text{mrad}), & \pi, \eta \end{cases} \tag{2.3.19}$$

Using the spectra of mesons (see Appendix 2.B), we find

$$\frac{\epsilon_{\text{geom}}^{\text{SND@LHC}}}{\epsilon_{\text{geom}}^{\text{FASER}}} \simeq \begin{cases} 1, & \pi, \eta, \\ \frac{\Omega_{\text{SND@LHC}}}{\Omega_{\text{FASER}}} \approx 5, & D, B, \tau \end{cases} \tag{2.3.20}$$

2.3.4.2 Decays

Based on these findings, we can make a simple comparison of minimal couplings that may be probed by the FASER and SND@LHC experiments. Further, we will assume the most optimistic estimate for SND@LHC, according to which decays of FIPs may be clearly distinguished from backgrounds, and therefore, only 3 events are required at 95% CL.

In the regime $l_{\text{decay}} \gg l_{\text{max}}$, the number of decay events of particles that originate from mesons is

$$N_{\text{decay}} \propto \epsilon_{\text{geom}} \cdot l_{\text{det}} \cdot g^4 \cdot \text{Br}_{\text{vis}} \tag{2.3.21}$$

From this relation, we obtain

$$\frac{g^2_{\text{lower,SND@LHC}}}{g^2_{\text{lower,FASER}}} \sim \sqrt{\frac{\gamma_X^{\text{SND@LHC}}}{\gamma_X^{\text{FASER}}}} \cdot \sqrt{\frac{\text{Br}_{\text{vis}}^{\text{FASER}}}{\text{Br}_{\text{vis}}^{\text{SND@LHC}}}} \cdot \begin{cases} 1.7, & \text{particles from } \pi, \eta \\ 0.8, & \text{particles from } D,\, B \end{cases} \tag{2.3.22}$$

where we used $l_{\text{det}}^{\text{SND@LHC}} = 0.5\,\text{m}$.

Therefore, assuming that SND@LHC may reconstruct decay events in background-free regime, the reaches of SND@LHC and FASER to probe decays of particles are comparable.

Comparing the lower bounds of the numerical sensitivities of SND@LHC and FASER for dark photons and dark scalars in Fig. 2.26, we find that they agree with the estimates (2.3.22). However, for HNLs there is a disagreement as large as a factor of 3. A

[15] Some of these approaches suffer from theoretical uncertainties in far-forward direction [162]: small p_{T} and large pseudorapidity require using parton distribution functions in the domain of small Bjorken scaling variable x, which are poorly constrained. One of the goal SND@LHC and FASER may serve for checking the distributions (and in particular the property (2.3.19)) via studying the events with neutrinos produced in the meson decays.

reason for this may be different distributions of D mesons used in our analysis and in [67] (see also Appendix 2.B).

Let us now comment on the lower bounds ratio with the upgrade. With the help of the formulas (2.3.20), (2.3.22) and table 2.4, we conclude that the FASER2 experiment has much better potential:

$$\frac{g^2_{\text{lower,SND@LHC upgr}}}{g^2_{\text{lower,FASER2}}} \simeq 20 \cdot \sqrt{\frac{\gamma_X^{\text{SND@LHC}}}{\gamma_X^{\text{FASER}}}} \cdot \sqrt{\frac{\text{Br}_{\text{vis}}^{\text{FASER}}}{\text{Br}_{\text{vis}}^{\text{SND@LHC}}}} \tag{2.3.23}$$

A reason for this is mainly significantly larger angular coverage in the case of the FASER2.

2.3.4.3 Scattering

Consider now the scattering signature. For the leptophobic portal, from Eq. (2.3.9), the ratio of minimal probed couplings is (for $\alpha_\chi = \alpha_B$)

$$\frac{\alpha_{B,\text{FASER}\nu}}{\alpha_{B,\text{SND@LHC}}} \sim \left(\frac{\epsilon_{\text{geom}}^{\text{FASER}\nu}}{\epsilon_{\text{geom}}^{\text{SND@LHC}}} \frac{l_{\text{det}}^{\text{FASER}\nu}}{l_{\text{det}}^{\text{SND@LHC}}} \frac{\sigma(E_{\text{threshold}}^{\text{FASER}\nu})}{\sigma(E_{\text{threshold}}^{\text{SND@LHC}})} \sqrt{\frac{N_{\nu\,\text{bg}}^{\text{FASER}\nu}}{N_{\nu\,\text{bg}}^{\text{SND@LHC}}}} \right)^{\frac{1}{3}} \tag{2.3.24}$$

where $N_{\nu\,\text{bg}}$ is the number of neutrino background events (different for the elastic and inelastic signatures), and we assume that the detection efficiency is equal to one. The effective cross section $\sigma(E_{\text{threshold}})$ depends on momentum threshold for charged particles to be visible. The dependence of σ on $E_{\text{threshold}}$ is very important for the elastic signature, as most of the elastic scattering events are characterized by low momenta. For the inelastic signature, it is less relevant. For SND@LHC, the requirements are $E_{\text{threshold}} = 170\,\text{MeV}$ for protons and $100\,\text{MeV}$ for other charged particles. For FASERν (Ref. [163]), we have not found the information about $E_{\text{threshold}}$. Instead, we assume $E_{\text{threshold}} = 1\,\text{GeV}$ that was used for the pilot run in 2018 (see also [164], where $300\,\text{MeV}$ cut is considered for FASERν2).

For small masses $m_V \lesssim 0.5$, the mediator is mainly produced from π, η decays, as shown in Fig. 2.24. In this case, we have $\epsilon_{\text{geom}}^{\text{SND@LHC}}/\epsilon_{\text{geom}}^{\text{FASER}\nu} \approx 0.3$. A similar increase occurs for $N_{\nu\,\text{bg}}$, since neutrinos are abundantly produced in decays of pions, and therefore, we can use the same scaling for the total neutrino events, $N_{\nu\,\text{bg}} \propto \epsilon_{\text{geom}} l_{\text{det}}$. The estimate then reads:

$$\frac{\alpha_{B,\text{SND@LHC}}}{\alpha_{B,\text{FASER}\nu}} \sim 9.6^{1/6} \left(\frac{\sigma(E_{\text{cut}}^{\text{SND@LHC}})}{\sigma(E_{\text{cut}}^{\text{FASER}\nu})} \right)^{-\frac{1}{3}} \simeq 1.5 \begin{cases} 1, & \text{inelastic} \\ 0.2 - 0.9, & \text{elastic} \end{cases} \tag{2.3.25}$$

We conclude that sensitivities of SND@LHC and FASER to scatterings are also comparable.

2.3.5 Conclusions

In this section, we have demonstrated the potential of the SND@LHC experiment to probe feebly interacting particles. We have considered scattering signatures and some decay signatures as well.

Light dark matter particles coupled via mediators may be searched by looking at the scattering signature, see Sec. 2.3.2.2. These events need to be distinguished from neutrino scatterings. Because of large mass of Z and W bosons that mediate the neutrino interactions, the neutrino scattering occurs inelastically most of the times. This may be not the case for light dark matter particles interacting via a light $\mathcal{O}(1\,\mathrm{GeV})$ mediator, for which the yields of elastic and inelastic scattering events are comparable (see Fig. 2.20). Therefore, looking for an excess in the yield of elastic scattering events is suitable for probing such FIPs. For heavier mediators, FIPs scattering still may be searched via an increase in the ratio of scattering events with a lepton and those without a lepton. On one hand, this ratio may be accurately measured at SND@LHC. On the other hand, it is clearly predicted by the SM. We have illustrated the power of these two signatures by estimating the sensitivity to the scattering of light dark sector particles via the leptophobic portal, see Fig. 2.25.

SND@LHC detector may also search for decays of mediators, see Sec. 2.3.4.2. Because of good spatial resolution of the emulsion in SND@LHC, decays into two charged particles may be distinguished from the neutrino scattering events. Such decays are main decay channel in the case of heavy neutral leptons, dark scalars that mix with Higgs boson, and dark photons. It is possible to probe their parameter space at its upgraded version as described in [32], see Fig. 2.26. However, further studies of possible backgrounds are required to clarify these results.

We have also compared the potential of SND@LHC and FASER/FASERν facilities to probe new physics, see Sec. 2.3.4. Placed at the same distance but at the opposite sides of the ATLAS experiment interaction point, they are very similar. There are a few factors, however, leading to differences in the sensitivity of these facilities to new physics. First, FASER is on-axis, while SND@LHC is slightly off-axis. The off-axis placement decreases the mean momentum of particles produced in the direction of SND@LHC, which somewhat worsens its potential to probe short-lived particles with the decay lengths of the order of the distance to the detector. Second, SND@LHC covers $\simeq 5$ times larger solid angle than FASER. Because of this, depending on the FIPs production channel, a fraction of FIPs flying in the direction of FASER is smaller than that for SND@LHC. For scatterings, FASERν has higher event rate due to larger detector length and on-axis position, resulting in better sensitivity. This can be applied for the inelastic signature; for other possible signatures, e.g. elastic scattering off protons, SND@LHC might have better sensitivity thanks to its higher momentum resolution.

Appendix

2.A CHARM sensitivity based on number of decay events estimate

The number of decay events for the pure α mixing at CHARM is given by the formula

$$N_{\text{events}}^{(\alpha)} = \sum_{X=D,\tau} N_X \cdot \text{Br}(X \to N_\alpha) \times \\ \times \int dE d\theta dz \cdot f_{N_\alpha}^X(E,\theta) \frac{e^{-l(z)/c\tau_N \gamma}}{c\tau_N^{(\alpha)}\gamma} \frac{\Delta\phi(\theta,z)}{2\pi} \cdot \epsilon_{\text{decay}}(\theta,z,E) \cdot \text{Br}(N_\alpha \to l\bar{l}') \cdot \epsilon_{\text{det},ll'} \tag{2.A.1}$$

Here,

$$N_{D_i} = N_{\text{PoT}} \times \chi_{c\bar{c}} \times f_{c\to D_i}, \quad N_\tau = N_{D_s} \times \text{Br}(D_s \to \tau\bar{\nu}_\tau) \tag{2.A.2}$$

are the total numbers of D mesons ($D_i = D_s, D^+, D^0$) and τ leptons, with $N_{\text{PoT}} = 2.4 \cdot 10^{18}$ being the total number of proton-target collisions at CHARM and $\chi_{c\bar{c}} \approx 4 \cdot 10^{-3}$ the production fraction of the $c\bar{c}$ at SPS energies for a thick target [44]. $\text{Br}_{D_s\to\tau} \approx 5.43\%$ [52] and $f_{c\to D_i}$ are given from [80]. $f_{N_\alpha}^X$ is the distribution of HNLs produced in decays of X particles in polar angle and energy. $z \in (480, 515)\,\text{m}$ is the longitudinal distance, $\theta \in (3.5/515, 6.5/515)$ is the polar angle coverage of the end of the CHARM's decay volume, while $\Delta\phi(\theta)/2\pi$ is the azimuthal acceptance for HNLs decaying inside the decay volume. ϵ_{decay} is the decay acceptance – a fraction of decay products of HNLs that both point to the detector. Finally, $\epsilon_{\text{det},ll'}$ are reconstruction efficiencies for leptonic decays: $\epsilon_{ee} \approx 60\%$, $\epsilon_{\mu\mu} \approx 75\%$, and $\epsilon_{e\mu} \approx 65\%$, which we use from [62].

Computing of $f_{N_\alpha}(E,\theta)$ requires knowing the distribution of D mesons and τ leptons $f_\tau(E,\theta)$ produced at the CHARM target. We approximate f_τ by the distribution of D_s mesons, while for the distribution of D mesons we use FairShip simulations [44] for collisions of the SPS proton beam with a thick Tungsten target.[16] The distribution of HNLs $f_{N_\alpha}^X(E,\theta)$ has been obtained from $f_X(E,\theta)$ semi-analytically using the method from [120].

We have estimated ϵ_{decay} by using a toy simulation for decays of HNLs inside the decay volume into three massless particles, and requiring the momenta of the two charged leptons to point towards the end of the decay volume. The acceptances are shown in Fig.2.27.

[16] Although at CHARM the target material is different, we believe that it is still a reasonable approximation.

In order to obtain the excluded domain, we assume the absence of background and require $N_{\text{events}} > 2.3$, which corresponds to the 90% C.L.

The comparison of this estimate with the rescale from Sec. 2.1.4 and [63] is shown in Fig. 2.27. We find that the estimates are in very good agreement. We also show our estimate of the CHARM bounds on the e mixing, which differs from the bounds obtained from [62] by including the production from D_s mesons, which dominates masses $m_N \gtrsim 700\,\text{MeV}$ (see also Fig. 2.5). The resulting sensitivity at the lower bound improves by up to a factor $3-4$ for this mass region.

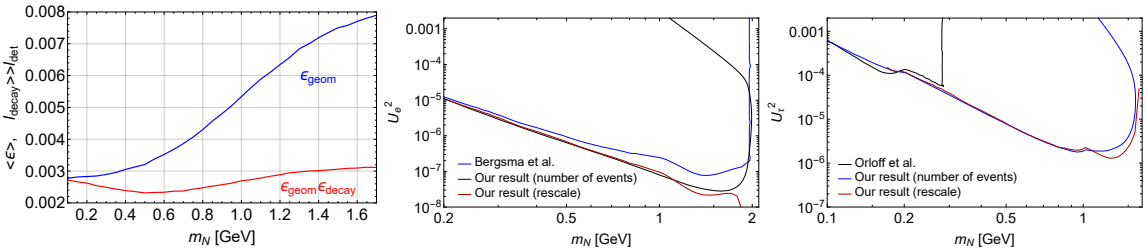

Figure 2.27: The left panel: fraction of HNLs that point towards the detector (blue line) and fraction of HNLs whose decay products point towards the detector (red line). The middle and right panels: comparison of our estimates of the constraint from the CHARM experiment on the pure e (the middle panel) and τ mixing (the right panel), with bounds reported in [62] and [63]. We show two estimates: the red line corresponds to the rescale of the bound on the e mixing from [62] (see Sec. 2.1.4 for details), while the blue line is our independent estimate based on Eq. (2.A.1).

2.B Decay events at SND@LHC

We estimate the number of decays using the following formula:

$$N_{\text{events}} = \sum_{\text{i}} N^i_{\text{prod}} \cdot \epsilon^i_{\text{geom}} \cdot P^i_{\text{decay}} \cdot \text{Br}_{\text{vis}}, \tag{2.B.1}$$

Here, N^i_{prod} is the total number of particles X produced via a channel i, ϵ_{geom} is the geometric acceptance, and P_{decay} is the decay probability averaged over energies of X,

$$P^i_{\text{decay}} = \int (e^{-l_{\text{min}}/c\tau_X\gamma_X} - e^{-l_{\text{max}}/c\tau_X\gamma_X}) f^i_{E_X} dE_X, \tag{2.B.2}$$

Here, $l_{\text{min}} = 480\,\text{m}$ is the distance to the SND@LHC detector, $l_{\text{max}} - l_{\text{min}} = l^{\text{decay}}_{\text{det}}$, f_{E_X} is the energy distribution of particles X that fly in the decay volume. Finally, Br_{vis} is the branching ratio of visible decays.

HNLs that mix with ν_μ are produced in decays of $D_s/D^{+/0}$ mesons. HNLs that mix with ν_τ are produced mainly in decays of τ-leptons, which, in their turn, originate from decays $D_s \to \tau\bar{\nu}_\tau$ [39]. We have obtained the distribution of D mesons using SIBYLL

2.3c [161, 165] as a part of the CRMC package [153]. As a cross-check, for the charm production we have compared the predictions of SIBYLL with results of the FONLL program [40, 42, 43]. We have found that the results agree well for angles $\theta > 0.8$ mrad.[17] Having the D distribution, we have obtained the distribution of τ-leptons and, subsequently, HNLs angles and momenta using the approach described in [120]. For simplicity, we approximate the angle-momentum distribution of HNLs by that of particles produced in a two-body decay $\tau \to \pi N$ (for the mixing with ν_τ) and $D_s \to \mu N$ (for the mixing with ν_μ).

Dark photons V in sub-GeV mass range are produced in decays $h = \gamma V$ of π- and η-mesons, and by proton bremsstrahlung [134]. We use the angle-energy distributions of the mesons generated by EPOS-LHC [152] as a part of the CRMC package [153], and follow [134] for the bremsstrahlung.

Dark scalars S are produced in decays $B \to X_s S$ of B-mesons, where X_s is a hadron including an s-quark, and by the proton bremsstrahlung [38]. We use FONLL in order to obtain the angle-energy distribution of B-mesons, and follow [38] for the proton bremsstrahlung.

Using the obtained distribution, we have reproduced the sensitivity of FASER to scalars and dark photons from [67]. However, we have not reproduced the sensitivity to HNLs, see Fig. 2.28. A reason may be in different distributions of D_s-mesons used in the estimates.

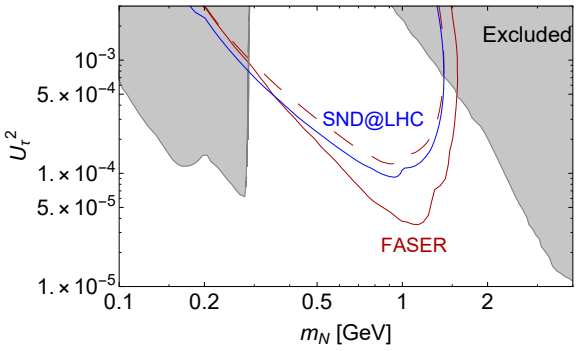

Figure 2.28: The sensitivity of FASER to HNLs that mix with ν_τ. The solid line corresponds to the contour given in Ref. [67], while the dashed line – to our estimate. For the comparison, we also show the sensitivity of SND@LHC (in blue).

2.C Leptophobic mediator: production, decays and scatterings

2.C.1 Production and decay

In order to describe interactions of V with hadrons, we follow [166] (see also [150]), in which vector mesons m play the role of gauge bosons of a "hidden" local $SU_f(3)$ symmetry in the space of pseudoscalar mesons nonet. The EM field is included as a background field

[17] For smaller angles, FONLL (both the online form and installed program) predicts zero or negative cross sections, which indicates some internal problem.

that is associated with the appropriate generator $Q = \text{diag}\left(\frac{2}{3}, -\frac{1}{3}, -\frac{1}{3}\right)$, and mix with the vector mesons. The coupling of the vector mesons to the pseudoscalar mesons is fixed by the anomalous decay $\pi^0 \to \gamma\gamma$. This model is very successful in describing the EM scattering data $e^+e^- \to$ hadrons and decay widths of vector mesons. We assume that it may be also used for describing the phenomenology of the leptophobic boson.

For the lephophobic mediator, the generator is $T_V = \frac{\not{V}}{3}$, and its mixing coupling is given by

$$f_{Vm} = -2g_B g_m \text{Tr}[T_V T_m], \tag{2.C.1}$$

where T_m is a generator associated with the given meson, and $g_m/m_m^2 = 1/\sqrt{12\pi}$, as fixed by the anomaly. The mixing occurs only with isosinglet ω- and ϕ-mesons, for which

$$T_\omega = \frac{1}{2}\text{diag}(1,1,0), \quad T_\phi = \frac{1}{\sqrt{2}}\text{diag}(0,0,1) \tag{2.C.2}$$

The decay width of V may be extracted from the experimental data on the EM ratios $\sigma(e^+e^- \to \text{hadrons})/\sigma(e^+e^- \to \mu^+\mu^-)$, where the hadronic final states correspond to ϕ-like and ω-like decays. This has been made in [144], in which the data have been used for describing the decay widths up to masses $m_V \simeq 1.7\,\text{GeV}$, while for larger masses perturbative calculations were used. We use the results of this paper.

The resonant enhancement is also important when considering the production of the mediator by the proton bremsstrahlung by affecting the form-factor F_{ppV} in the ppV vertex. The baryonic form factor F_{ppV} may be related to the proton and neutron EM dipole form-factors $F_{p/n}$, which are, in its turn, related to the isoscalar form factor $F_\omega \equiv \frac{F_p+F_n}{2}$, which in the extended vector meson dominance model coincides with the ω contribution [154]:[18]

$$\langle p|J_B|p\rangle = \langle p|J_{\text{EM}}|p\rangle + \langle n|J_{\text{EM}}|p\rangle \longrightarrow F_{ppV} = 2F_\omega \tag{2.C.3}$$

Unfortunately, the experimental data on $e^+e^- \to p^+p^-$, which may be used for extracting the EM form-factors in the time-like region, is limited by the physical threshold $q^2 > 4m_p^2$. Following [154] (see also [151]), for extrapolating in the domain of lower invariant masses we use

$$F_{ppV}(q^2) = \sum_\omega f_\omega \frac{m_\omega^2}{m_\omega^2 - q^2 - i\Gamma_\omega m_\omega}, \tag{2.C.4}$$

where the sum goes over $\omega(782), \omega(1420), \omega(1680)$, $f_\omega = 2f_{NN\omega}/g_\omega$, with $f_{NN\omega}$ being the meson's coupling to the nucleon, while g_ω is the meson's coupling to photon. We use the couplings $f_{NN\omega(782)} = 17.2$ and $g_{\omega(782)} = 17.1$ [154]. The couplings to the other two resonances are unknown. However, the remaining two coefficients $f_{\omega(1420)} = -2.16 + 0.77i$ and $f_{\omega(1680)} = 1.14 - 0.57i$ in Eq. (2.C.4) may be fixed by two requirements: $F_{ppV}(0) = 1$, and $F_{ppV}(-q^2) \sim 1/q^4$. The first requirement comes from the fact that the form-factor F_{ppV}

[18] We assume no contribution of the ϕ-meson to the form-factor, since the corresponding coupling $f_{\phi NN}$ is expected to be suppressed [167, 168] (i.e., neglecting the s-quark contribution in the proton PDF).

is reduced to the baryon charge at low momenta transfer. The second requirement comes from the behavior of the proton's dipole form-factor in the space-like region predicted by the quark counting rules [169].

The behavior of the branching ratio into a $\chi\chi$ pair and the form-factor is shown in Fig. 2.29. Note that for the choice $\alpha_\chi = \alpha_B$, commonly considered in the literature, the enhancement of F_{ppV} near $m_V = m_{\omega(770)}$ and suppression of $\text{Br}(V \to \chi\chi)$ due to the ω resonances cancel each other.

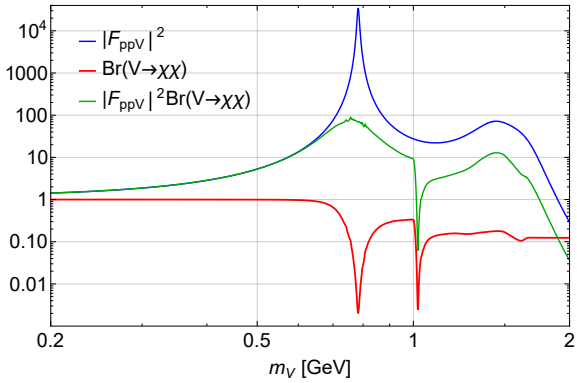

Figure 2.29: The behavior of the ppV form-factor (2.C.4) and the branching ratio for the process $V \to \chi\chi$. The coupling $\alpha_\chi = \alpha_B$ is assumed, and $m_\chi = m_V/3$.

2.C.2 Elastic and inelastic scattering cross sections

2.C.2.1 Elastic scattering

The cross section of the elastic scattering is

$$\sigma_{\text{elastic}} = \int dE_\chi f_{E_\chi} \int_{E_{N,\min}}^{E_{N,\max}(E_\chi)} dE_N \frac{d\sigma_{\chi N \to \chi N}}{dE_N}, \tag{2.C.5}$$

where $E_{N,\min}$ is the minimal recoil energy that may be detected, the maximal recoil energy of the nucleon is

$$E_{N,\max} = \frac{m_N(2E_\chi^2 + 2E_\chi m_N + m_N^2 - m_\chi^2)}{2E_\chi m_N + m_N^2 + m_\chi^2}, \tag{2.C.6}$$

$Q^2 = 2m_N(E_N - m_N)$ is the modulus of the squared momentum transfer, $Q^2 = -(p_\chi - p'_\chi)^2$. Finally, the differential cross section is

$$\frac{d\sigma_{\chi N \to \chi N}}{dE_N} = 4\pi\alpha_D^2 F_N(Q^2) \frac{m_N(2E_\chi^2 + 2E_\chi m_N + m_\chi^2) - E_N(2E_\chi m_N + m_\chi^2)}{(E_\chi^2 - m_\chi^2)(2E_N m_N - 2m_N^2 + m_V^2)^2}, \tag{2.C.7}$$

where $F_N(Q^2)$ is the elastic form-factor, which we assume to be $F_N(Q^2) = \frac{1}{(1+\frac{Q^2}{0.71\,\text{GeV}^2})}$.

2.C.2.2 Inelastic scattering

In the case of the inelastic scattering, we follow [148], which uses the parton model. Let us introduce the variables $E_V = E_\chi - E_\chi^{'}$, Q^2. The differential cross section is

$$\frac{d^2\sigma}{dE_V dQ^2} = \frac{\pi\alpha_D^2}{9m_N}\frac{1}{E_\chi^2 - m_\chi^2}\frac{1}{(m_V^2+Q^2)^2}(2p-q)^\mu(2p-q)^\nu W_{\mu\nu}\sum_q x f_q(x,Q^2), \quad (2.C.8)$$

where $f_q(x,Q^2)$ is the parton distribution function ($q = u/\bar{u}/d/\bar{d}/s/\bar{s}$), $x = \frac{Q^2}{2m_N E_V}$, $W_{\mu\nu}$ is the hadronic tensor,

$$W_{\mu\nu} = -g_{\mu\nu} + \frac{q_\mu q_\nu}{q^2} + \frac{2x}{p_N\cdot q + 2xm_N^2}\left(p_{N\mu} - \frac{p_N\cdot q}{q^2}q_\mu\right)\left(p_{N\nu} - \frac{p_N\cdot q}{q^2}q_\nu\right) \quad (2.C.9)$$

Because of the property $q^\mu W_{\mu\nu} = q^\nu W_{\mu\nu} = 0$, we have

$$(2p-q)^\mu(2p-q)^\nu W_{\mu\nu} = \frac{4E_\chi^2Q^2 - 4E_V E_\chi Q^2 - Q^4}{E_V^2+Q^2} - 4m_\chi^2 \quad (2.C.10)$$

The kinematic limits are

$$Q^2 < 2m_N E_V, \quad 2\mu^2 < Q^2 < 4(E_\chi(E_\chi - E_V) - m_\chi^2) - 2\mu^2, \quad (2.C.11)$$

$$E_{\text{min}} < E_V < \frac{2m_N(E_\chi^2 - m_\chi^2)}{2E_\chi m_N + m_N^2 + m_\chi^2}, \quad (2.C.12)$$

where E_{min} is the minimal recoil, and the function μ is

$$\mu^2 = \frac{m_\chi^2 E_V^2}{E_\chi(E_\chi - E_V) - m_\chi^2 - \sqrt{(E_\chi(E_\chi-E_V)-m_\chi^2)^2 - m_\chi^2 E_V^2}} \quad (2.C.13)$$

To get $f_q(x,Q^2)$, we use LHAPDF with CT10nlo PDF sets. We assume that they are zero if $Q < 1\,\text{GeV}$.